

# The Effect of Noise and Lipid Signals on Determination of Gaussian and Non-Gaussian Diffusion Parameters in Skeletal Muscle

Donnie Cameron, Ph.D.<sup>1,2</sup>

Mustapha Bouhrara, Ph.D.<sup>1†</sup>

David A. Reiter, Ph.D.<sup>1†</sup>

Kenneth W. Fishbein, Ph.D.<sup>1</sup>

Seongjin Choi, Ph.D.<sup>1</sup>

Christopher M. Bergeron, A.S.<sup>1</sup>

Luigi Ferrucci, M.D., Ph.D.<sup>1\*</sup>

Richard G. Spencer, M.D., Ph.D.<sup>1\*</sup>

<sup>1</sup>*National Institute on Aging, National Institutes of Health, Baltimore, Maryland, USA.*

<sup>2</sup>*Norwich Medical School, University of East Anglia, Norwich, UK.*

†,\* These authors contributed equally to this work.

**Corresponding Author Info:** Richard G. Spencer, M.D., Ph.D., NIH/National Institute on Aging, Intramural Research Program, BRC 04B-116, 251 Bayview Boulevard, Baltimore, MD 21224. E-mail: [spencer@helix.nih.gov](mailto:spencer@helix.nih.gov).

**Word Count:** 4999

**Grant Support:** This work was supported entirely by the Intramural Research Program of the NIH, National Institute on Aging.

**Keywords:** diffusion-weighted imaging, non-Gaussian diffusion, fat suppression, muscle, parameter estimation.

**Abbreviations Used:**

*ADC* – apparent diffusion coefficient

1  
2  
3  $\alpha$  – stretching parameter

4  
5  
6 BMI – body mass index

7  
8  $D^*$  – pseudo-diffusion coefficient

9  
10  $DDC$  – distributed diffusion coefficient

11  
12  
13 DWI – diffusion-weighted imaging

14  
15 EPI – echo planar imaging

16  
17  
18  $f_d$  – diffusion fraction

19  
20  
21  $f_d'$  – corrected diffusion fraction

22  
23  
24  $f_p$  – perfusion fraction

25  
26  
27  $f_p'$  – corrected perfusion fraction

28  
29 IVIM – intravoxel incoherent motion

30  
31  
32  $K$  – kurtosis

33  
34 LA – limits of agreement

35  
36 MD – mean difference

37  
38  
39 mDIXON – multiecho two-point Dixon

40  
41 RMSE – root-mean-square error

42  
43 ROI – region of interest

44  
45  
46 SX – stretched exponential

47  
48 SENSE – sensitivity encoding

49  
50  
51 SNR – signal-to-noise ratio

52  
53 SPAIR – spectral attenuated inversion recovery

54  
55 SSGR – slice-select gradient reversal

56  
57  
58 WSE – water-specific excitation

## ABSTRACT SUMMARY

This work characterizes the effect of lipid and noise signals on muscle diffusion parameter estimation in several conventional and non-Gaussian models, the ultimate objectives being to characterize popular fat suppression approaches for human muscle diffusion studies, to provide simulations to inform experimental work, and to report normative non-Gaussian parameter values. The models investigated in this work were the Gaussian monoexponential and intravoxel incoherent motion (IVIM) models, and the non-Gaussian kurtosis and stretched exponential models. These were evaluated via simulations, and in vitro and in vivo experiments. Simulations were performed using literature input values, modeling fat contamination as an additive baseline to data, while phantom studies used a phantom containing aliphatic and olefinic fats and muscle-like gel. Human imaging was performed in the hamstring muscles of ten volunteers. Diffusion-weighted imaging was applied with spectral attenuated inversion recovery (SPAIR), slice-select gradient reversal, and water-specific excitation fat suppression, alone and in combination. Measurement bias (accuracy) and dispersion (precision) were evaluated, along with intra- and interscan repeatability. Simulations indicated that noise in magnitude images resulted in <6% bias in diffusion coefficients and non-Gaussian parameters ( $\alpha$ ,  $K$ ), while baseline fitting minimized fat bias for all models, except IVIM. In vivo, popular SPAIR fat suppression proved inadequate for accurate parameter estimation, producing non-physiologic parameter estimates without baseline fitting and large biases when it was used. Combining all three fat suppression techniques and fitting data with a baseline offset gave the best results out of the methods studied for both Gaussian diffusion and, overall, for non-Gaussian diffusion. It produced consistent parameter estimates for all models, except IVIM, and highlighted non-Gaussian behavior perpendicular to muscle fibers ( $\alpha \sim 0.95$ ,  $K \sim 3.1$ ). These results show that effective fat suppression is crucial for accurate measurement of non-Gaussian diffusion parameters, and will be an essential component of quantitative studies of human muscle quality.

## INTRODUCTION

Diffusion-weighted imaging (DWI) has been used as a non-invasive probe of human tissue ultrastructure (1, 2), with the conventional diffusion model, in which signal intensity decays monoexponentially as a function of  $b$ -value, being the most well-studied. However, non-monoexponential, ‘non-Gaussian’ diffusion models may better reflect complex tissue architecture (3). For example, multi-exponential models describe multiple monoexponential diffusion components, each with its own signal fraction and decay constant, while kurtosis and stretched exponential (SX) models can characterize a continuum of diffusion components, with component amplitudes described by a probability distribution. Description in terms of non-Gaussian diffusion may be particularly appropriate for skeletal muscle, given that it exhibits restrictive cellular architecture, and develops microstructural changes in response to resistance training, pathologies, and age-related sarcopenia (4, 5). Clearly, this approach shows great potential for studying skeletal muscle ultrastructure, though the current literature is sparse (6, 7).

When applying new diffusion analysis models, it is important to consider possible sources of error in parameter estimation. Noise has a deleterious effect on diffusion parameter estimation, as has been demonstrated for Gaussian models (8-10) and, to a limited extent, for non-Gaussian models (11). However, a heretofore neglected area of study is the effect of lipid signals on non-Gaussian diffusion models. Fat poses two main problems for diffusion analysis in muscle: first of all, improperly suppressed lipids dominate the diffusion-weighted signal at high  $b$ -values and result in underestimation of monoexponential water diffusivity (12); and secondly, even with optimal fat suppression, water present in adipose tissue can give rise to partial volume effects and associated errors (9, 13, 14). The former of these two effects is frequently overlooked, and will receive thorough treatment here.

Lipid signals are difficult to suppress in DWI, particularly when  $B_0$  homogeneity is poor, and the low-bandwidth sampling intrinsic to the use of echo-planar imaging (EPI) readouts leads to spatially misregistered lipid signals that obscure the anatomy of interest. There are multiple lipid resonances, including aliphatic fat from 1.2–3.0 ppm and olefinic fat at 5.3 ppm, necessitating suppression of several species, one of which is close to the water resonance. Fortunately, many techniques are available for suppressing these signals, including frequency-selective methods like spectral attenuated inversion recovery (SPAIR)(15), water-specific

excitation (WSE)(16), and slice-select gradient reversal (SSGR)(17). Each technique offers different strengths, with associated costs: WSE excites only water and adjacent olefinic fat resonances, at the expense of increased slice thickness and TE; SPAIR effectively suppresses most aliphatic fat, while extending the minimum TR; and SSGR partially suppresses both olefinic and aliphatic fat, at no added cost. It is already clear from these brief considerations that the signal from olefinic fat, while approximately a factor of ten smaller in amplitude than that of aliphatic fat, is more resistant to conventional fat-suppression techniques due to its proximity to the water resonance. However, advanced methods for eliminating olefinic fat have recently been reported (18, 19).

The objective of this work is twofold. Firstly, we experimentally investigate optimization of fat-suppression for DWI using three readily-implemented techniques: WSE, SPAIR, and SSGR. Secondly, we explore the effect of noise and lipid signals on parameter estimates in monoexponential, stretched exponential, kurtosis, and intravoxel incoherent motion (IVIM) diffusion models, via extensive numerical simulations. The results of these investigations will guide the experimentalist in their choice of DWI fat suppression methods and analysis models, as well as providing normative diffusion parameter estimates in healthy skeletal muscle.

## THEORY

### Candidate Diffusion Models

The functional forms for the models evaluated are:

- *Monoexponential*:

$$S = S_{0,\text{muscle}} \exp(-bADC) + \varepsilon, \quad (1)$$

where  $S$  is the observed signal,  $S_{0,\text{muscle}}$  is the signal from muscle at  $b = 0$ ,  $ADC$  is the apparent diffusion coefficient, and  $\varepsilon$  is a baseline offset used to mitigate bias from residual fat.

- *Stretched exponential (SX)*:

$$S = S_{0,\text{muscle}} \exp\left(-\left(bDDC\right)^\alpha\right) + \varepsilon, \quad (2)$$

where  $DDC$  is the distributed diffusion coefficient and  $\alpha$  is the stretching parameter, with  $0 \leq \alpha \leq 2$  (20). This model reduces to a monoexponential for  $\alpha = 1$ , with  $\alpha < 1$  indicating subdiffusive behavior and  $\alpha > 1$  superdiffusive behavior.

• *Kurtosis:*

$$S = S_{0,\text{muscle}} \exp\left(-bDDC + b^2 DDC^2 (K - 3)/6\right) + \varepsilon, \quad (3)$$

where  $K$  is kurtosis, with  $K \geq 1$ , and  $K = 3$  indicates monoexponential diffusion. This definition permits calculation of relative errors, unlike the ‘excess’ kurtosis definition, where  $K_{\text{excess}} = K - 3$  and  $K_{\text{excess}} = 0$  represents monoexponential diffusion.

• *Intravoxel incoherent motion (IVIM):*

$$S = S_{0,\text{muscle}} \left( f_p \exp(-bD^*) + 1 - f_p \exp(-bADC) \right) + \varepsilon, \quad (4)$$

a biexponential model where  $f_p$  is the perfusion fraction and  $D^*$  is the pseudo-diffusion coefficient (21). To account for blood-tissue relaxation time differences (22),  $f_p$  is corrected to  $f_p'$  as follows:

$$f_p'(\%) = \frac{f_p \cdot \frac{C_{\text{muscle}}}{C_{\text{blood}}}}{1 - f_p \left( 1 - \frac{C_{\text{muscle}}}{C_{\text{blood}}} \right)} \times 100, \quad (5)$$

where  $C_{\text{blood}}$  and  $C_{\text{muscle}}$  are relaxation correction factors for blood and muscle, given by

$$C_{\text{blood}} = \exp(-TE/T_{2,\text{blood}}) \cdot \left( 1 - \exp(-TR/T_{1,\text{blood}}) \right), \quad (6)$$

$$C_{\text{muscle}} = \exp(-TE/T_{2,\text{muscle}}) \cdot \left( 1 - \exp(-TR/T_{1,\text{muscle}}) \right), \quad (7)$$

with  $T_1$  and  $T_2$  of blood and muscle at 3T taken as  $T_{1,\text{blood}} = 1932$  ms,  $T_{2,\text{blood}} = 275$  ms,  $T_{1,\text{muscle}} = 1412$  ms, and  $T_{2,\text{muscle}} = 45$  ms, respectively (23). Once  $f_p'$  has been determined, the diffusion fraction,  $f_d$ , is simply corrected to  $f_d'$  by  $100 - f_p'$ .

### Accuracy, Precision, and Model Goodness-of-Fit

In this work, the accuracy and precision of diffusion model parameter estimates are reported as the relative bias and dispersion, respectively:

$$\text{Bias}(\%) = \frac{100}{N} \left( \sum_{i=1}^N x_i - x_{\text{ref}} \right) / x_{\text{ref}}, \quad (8)$$

$$\text{Dispersion (\%)} = \left( 100 \sqrt{\frac{1}{N-1} \sum_{i=1}^N (x_i - \bar{x})^2} \right) / \bar{x} \quad (9)$$

where  $x_i$  is the parameter value estimated for the  $i$ th noise realization,  $x_{ref}$  is the true value,  $\bar{x}$  is the mean of all estimates, and  $N$  is the number of noise realizations (24). The goodness-of-fit of each diffusion model is expressed as the root-mean-squared error:

$$\text{RMSE} = \sqrt{\frac{\text{RSS}}{n-k}}, \quad (10)$$

where  $n$  is the number of data points, RSS is the residual sum-of-squares, and the number of parameters,  $k$ , is included to adjust for the number of degrees of freedom. A smaller RMSE indicates better fit quality.

## METHODS

### Fitting Data

For all experiments, the monoexponential, SX, and kurtosis diffusion models were fit to data for  $b = 0, 276, 381, 525, 725, 1000, 1380, 1904, 2627, 3624,$  and  $5000 \text{ s/mm}^2$  using the 'lsqcurvefit' least-squares algorithm (MATLAB; MathWorks, Natick, USA). The muscle signal at  $b = 0$ ,  $S_{0,\text{muscle}}$ , was included as a fitted parameter for all models. A maximum  $b$ -value,  $b_{\text{max}}$ , of  $5000 \text{ s/mm}^2$  was chosen to improve baseline fitting (8), and to allow detection of the kurtosis model's quadratic term while neglecting higher-order terms (6, 25).

The IVIM model was fit to data for  $b = 0, 10, 18, 33, 60, 110, 276, 381, 525, 725,$  and  $1000 \text{ s/mm}^2$  using a multi-step approach whereby  $(1-f_p)$  and  $ADC$  were estimated by a linear fit to log-transformed, perfusion-free data ( $b$ -values highlighted in italics)(26), before being input to the biexponential fit as fixed terms.

In vitro and in vivo, diffusion signal decays were calculated from regions of interest (ROIs), and fit with Equations 1–4. Pixel-by-pixel parameter maps were calculated solely to visualize the spatial variation of parameters, and were not used for quantification.

## Numerical Simulations

Simulations were used to determine the effect of noise and fat on the accuracy and precision of diffusion parameter estimation in skeletal muscle. Firstly, diffusion signal decays were generated as per Equations 1–4, without offset  $\varepsilon$ , using the following input values:

- $ADC = 2.0 \times 10^{-3}$ ,  $1.5 \times 10^{-3}$ , and  $1.3 \times 10^{-3}$   $\text{mm}^2/\text{s}$ ,
- $DDC = 2.0 \times 10^{-3}$   $\text{mm}^2/\text{s}$ ,
- $K = 3.0$ ,  $3.3$ , and  $3.6$ ,

from the literature (5, 6); and values from previous work (27),

- $f_p = 15\%$ ,  $10\%$ , and  $5\%$ ,
- $D^* = 25.0 \times 10^{-3}$   $\text{mm}^2/\text{s}$ ,
- $\alpha = 1.0$ ,  $0.9$ , and  $0.8$ .

Constant baseline offsets,  $\varepsilon$ , were added to these data to produce fat signal fractions of 0–25%, in steps of 0.125%, relative to the fat-free  $b = 0$  signal amplitude (12). The range of fat fractions was chosen to correspond to values seen experimentally with typical DWI acquisitions. Constant offsets were used to reflect the fact that fat's  $ADC$  ( $\sim 2 \times 10^{-5} - 4 \times 10^{-5}$   $\text{mm}^2/\text{s}$ ) is approximately two orders of magnitude smaller than that of water (28).

For each fat fraction, zero-mean Gaussian noise, with standard deviation (SD)  $\sigma$ , was added to both the real and the imaginary parts of the complex signal to produce a range of SNRs, defined as  $S(0)/\sigma$ . Magnitude data were generated for  $\text{SNR} = 1-50$ , in steps of 0.25, each with 1000 noise realizations, and noiseless data were generated for the case of infinite SNR.

To investigate fitting functions for fat and noise compensation in DWI data, the monoexponential, SX, kurtosis, and IVIM models were also applied with no offset terms, with baseline offset  $\varepsilon$ , and with a baseline offset plus a noise parameter,  $\zeta$  (8), for a range of  $b_{\text{max}}$  values (see Supplementary Material).

## Magnetic Resonance Imaging

Imaging was conducted on a Philips Achieva 3.0T X-series system (Philips Healthcare, Best, The Netherlands) equipped with Quasar Dual gradients (80 mT/m maximum amplitude, 100 mT/m/ms slew rate), with a 32-channel cardiac coil for signal reception and a quadrature body coil for transmission.

The following scans were performed both in vivo and in vitro:

• *Multiecho two-point Dixon (mDIXON)*, to acquire high-resolution water and fat images (29); TR = 4.1 ms, TE = 1.5 and 2.7 ms, flip angle = 15°, field-of-view = 270 mm × 270 mm, in-plane resolution = 1 mm × 1 mm, slice thickness = 5 mm, and sensitivity encoding (SENSE) factor = 2.

• *Diffusion-weighted spin echo single-shot EPI*, with TR/TE = 3000/71 ms, field-of-view = 270 mm × 270 mm, in-plane resolution = 2.7 mm × 2.7 mm (reconstructed to 1.7 mm × 1.7 mm), slice thickness = 22 mm, 8 averages, partial Fourier factor = 0.6 in the phase-encoding direction, SENSE factor = 2, diffusion gradient duration  $\delta = 27$  ms and interval  $\Delta = 35$  ms, 16 logarithmically-spaced  $b$ -values (0, 10, 18, 33, 60, 110, 276, 381, 525, 725, 1000, 1380, 1904, 2627, 3624, and 5000 s/mm<sup>2</sup>), and diffusion sensitization in the slice and readout directions.

To evaluate fat suppression quality, a total of 16 DWI datasets were acquired, applying the following fat suppression configurations with diffusion sensitization in the slice and readout directions: (i) no fat suppression; (ii) SSGR; (iii) SPAIR; (iv) WSE; (v) SPAIR+SSGR; (vi) WSE+SSGR; (vii) WSE+SPAIR; and (viii) WSE+SPAIR+SSGR, with a binomial 1-4-6-4-1 WSE pulse, SPAIR delay = 200 ms, and SPAIR offset = 250 Hz. Fig. 1 illustrates all three fat suppression modules as they appeared in the sequence.

**Signal-to-Noise Determination.** To facilitate comparison of in vivo and in vitro data with simulations, DWI SNR was estimated using a  $b = 0$  image along with a noise reference scan acquired without RF or gradients:

$$\text{SNR} = \frac{\text{mean}(S(\mathbf{r}))}{\sqrt{\frac{2}{4-\pi}}} \cdot \text{SD}(N(\mathbf{r})), \quad (11)$$

as per Yu et al.(30), where  $S(\mathbf{r})$  is the signal intensity in pixel  $\mathbf{r} = (r_x, r_y, r_z)$  in a given ROI,  $N(\mathbf{r})$  the signal from the noise image, and  $\sqrt{2/(4-\pi)}$  the Rayleigh limit of Rician-distributed noise.

### General MRI Data Processing

All data processing was performed in MATLAB. To account for signal drift and eddy current effects (31, 32), in vitro and in vivo DWI data were registered to mDIXON images via an affine control-point algorithm. They were then masked using a composite water-fat image generated

1  
2  
3 from mDIXON water data and  $b = 5000 \text{ s/mm}^2$  DWI data, where the latter highlights shifted  
4 olefinic fat signals.  
5  
6  
7  
8

## 9 **In Vitro Experiments**

10 **Phantom Construction.** A two-chamber coaxial phantom, similar to that described by  
11 Winfield et al.(33), was constructed from polycarbonate plastic with dimensions approximating  
12 the cross-section of the human thigh: overall length = 135 mm, overall diameter = 150 mm, and  
13 inner chamber diameter = 119 mm. The inner cylinder was filled with an agarose gel (3% w/v,  
14 Sigma-Aldrich) containing nickel sulphate hexahydrate (0.4 mM, Sigma-Aldrich), sucrose (1.5%  
15 w/v, Sigma-Aldrich), and sodium chloride (9 g/l, J.T. Baker), to give an inner compartment with  
16  $T_1$  and  $T_2$  relaxation times (23), diffusivity (5), and conductivity similar to muscle tissue (34).  
17 The outer chamber was filled with corn oil (Mazola), to give a lipid spectrum similar to that of  
18 subcutaneous fat (33).  
19  
20  
21  
22  
23  
24  
25  
26  
27

28 **In-Vitro Imaging Protocol.** The phantom's long-axis was aligned with the magnet bore, and  
29 its  $B_0$  homogeneity was optimized using a projection-based shimming algorithm. Besides the  
30 mDIXON and DWI acquisitions, axial images were also obtained using the following sequences:  
31  
32  
33

- 34 • *Inversion recovery fast-spin-echo*, to measure the gel  $T_1$ ; TR/TE = 10000/10 ms, and TI =  
35 50, 75, 150, 300, 600, 1200, and 2400 ms, plus an acquisition without an inversion pulse to  
36 measure  $M_0$ .  
37  
38
- 39 • *Multiple spin echo*, to measure the gel  $T_2$ ; TR = 10000 ms and TE = 20–140 ms, in steps  
40 of 20 ms.  
41  
42  
43  
44

45 **Quality of Fat Suppression In Vitro.** All fat suppression configurations were applied in five  
46 separate scan sessions to assess variability, with the phantom being removed, repositioned, and  
47 reshimmmed between sessions. In a sixth session, a coarse, three-slice image-based shim (35) was  
48 applied over the whole phantom to produce broad spectral lines to challenge fat suppression.  
49 Each session lasted approximately 75 minutes.  
50  
51  
52

53 All fat suppression combinations were quantitatively assessed using ROIs drawn on  $b =$   
54  $1000 \text{ s/mm}^2$  images in areas where agarose gel and shifted aliphatic and olefinic fat signals  
55

1  
2  
3  
4  
5  
6  
7  
8  
9  
10  
11  
12  
13  
14  
15  
16  
17  
18  
19  
20  
21  
22  
23  
24  
25  
26  
27  
28  
29  
30  
31  
32  
33  
34  
35  
36  
37  
38  
39  
40  
41  
42  
43  
44  
45  
46  
47  
48  
49  
50  
51  
52  
53  
54  
55

appeared separately. Water and fat signal intensities were measured in these three ROIs and used to calculate mean and SD water:aliphatic-fat and water:olefinic-fat ratios over the five sessions.

To evaluate fat's influence on model parameter estimation, two additional ROIs were drawn in areas where shifted aliphatic and olefinic fat signals, respectively, overlaid the signal from agarose gel. For these, and the gel-only ROI, model parameters were estimated and their bias (Equation 8) was evaluated relative to estimates in well-shimmed, non-fat-suppressed gel—to avoid errors arising from perturbations of the water signal.

### **In Vivo Experiments**

All volunteers received a comprehensive description of the study, including possible risks, and gave informed consent according to the local Institutional Review Board guidelines.

***In Vivo Imaging Protocol.*** Participants were positioned feet-first, supine with the left thigh approximately at isocenter. A 10 cm bolster was placed under their knees to align the 'fusiform' hamstring muscles with the bore, minimizing angulation between hamstring muscle fibers and the prescribed diffusion sensitization directions. After localizers, the entire thigh was shimmed to second order using image-based shimming (35), and a single DWI slice was planned in the thickest part of the thigh, using WSE+SPAIR+SSGR fat suppression.

***Quality of Fat Suppression In Vivo.*** All fat suppression configurations were applied in 2 volunteers with distinctly different body habitus (both male, ages 30 and 51 years, BMI = 20 and 33, respectively), in order to create different fat suppression and  $B_0$  shimming challenges. These scans took approximately 75 minutes.

To determine fat's effect on parameter estimation in vivo, two additional ROIs were drawn in muscle overlaid with shifted subcutaneous aliphatic and olefinic fat signals, respectively. For these, and the muscle-only ROI, model parameters were estimated and their bias (Equation 8) was evaluated relative to WSE+SPAIR+SSGR-fat-suppressed muscle, in order to avoid bias from intramuscular fat.

***In Vivo Normative Diffusion Parameters and Repeatability.*** Fat-suppressed DWI data were obtained in 10 additional volunteers (all male, median age = 40, range = 27-78 years), with diffusion gradients applied in the slice direction in all 10, and in the readout direction in 8.

Intra- and inter-session repeatability of DWI were assessed for both diffusion directions in 5 of these participants, using Bland-Altman analysis. Participants were scanned twice in one session and again in a separate session within one week. Each scan lasted approximately 30 minutes.

## RESULTS

### Numerical Simulation Results

Analyses of fitting functions with no offset terms, with baseline offset  $\varepsilon$ , and with an offset plus noise parameter  $\xi$ , for multiple are shown in the Supplementary Material, along with the effects of the choice of  $b_{\max}$ .

Fig. 2 shows relative bias and dispersion of parameter estimates for each diffusion model as a function of fat fraction and SNR. At 0% fat fraction (bottom of each plot), the monoexponential, SX, and kurtosis models show similar bias and dispersion for estimating  $ADC$  or  $DDC$ , with each approaching an asymptote at  $SNR \sim 10$ . The stretching parameter,  $\alpha$ , shows similar biases to  $DDC$ , again with an asymptote at  $SNR \sim 10$ . Its dispersion, however, decreases more slowly for increasing SNR, and  $K$  showed an even shallower decrease in bias and dispersion as SNR increased. For the IVIM model,  $ADC$  and  $f_p$  show negative biases and large dispersions at  $SNR < 10$ , but the bias and dispersion of  $ADC$  approached those of the other models' diffusion coefficients above this threshold. The bias in  $D^*$  decreased with increasing SNR, though its dispersion was typically  $> 100\%$  for all perfusion fractions and simulated SNRs.

Assuming fat fraction = 0, at the level of in vivo SNR,  $\sim 40$ , each model showed less than 6% bias in diffusion coefficient estimation. IVIM parameters showed bias (dispersion): in  $f_p$ , -18 (153)% for a nominal  $f_p = 15\%$ , -26 (249)% for  $f_p = 10\%$ , and -50 (722)% for  $f_p = 5\%$ ; and for  $D^*$ , -18 (101)% for  $f_p = 15\%$ , -13 (138)% for  $f_p = 10\%$ , and -6 (161)% for  $f_p = 5\%$ . The SX model showed a bias (dispersion) in  $\alpha$  of  $\sim 6\%$  ( $\sim 8\%$ ), while kurtosis showed a bias (dispersion) of -14 (20)% for  $K = 3.0$ , -8 (12)% for  $K = 3.3$ , and -1 (1)% for  $K = 3.6$ .

As fat fraction increased, the bias in diffusion coefficients decreased at low SNRs, and dispersion increased monotonically. IVIM was markedly fat-sensitive: the bias in IVIM-estimated  $ADC$  was -66% for 25% fat, decreasing with increasing fat fraction due to skewing of the linear fit, which also led to smaller estimates of  $(1-f_p)$ . However, non-modeled fat signal simultaneously increased the apparent  $f_d$ , leading to large biases in  $f_p$  for each fat fraction. Finally,  $D^*$  showed a monotonic relationship with fat fraction, though the slope of this relationship changed sign as a function of SNR.

## In Vitro Results

**Quality of Fat Suppression In Vitro.** Example phantom DWI images acquired with each fat suppression method are presented in Fig. 3, alongside mDIXON images and parameter maps. Shifted aliphatic fat signals are prominent for all fat suppression configurations except WSE+SPAIR and WSE+SPAIR+SSGR, while shifted olefinic fat remains in all cases. Maps of  $f_p$  show that shifted fat signals produce a spurious perfusion component in the phantom.

Fig. 4 shows water-fat ratios in vitro. The mean (SD) water:aliphatic-fat was largest for WSE+SPAIR+SSGR, 75.6 (7.3), and marginally smaller for WSE+SPAIR, 73.7 (12.1); both methods showed significantly greater water-fat ratios than the other methods ( $p < 0.001$ ) without being significantly different from one another. Water:olefinic-fat was relatively constant in all cases, indicating the difficulty in suppressing olefinic fat along with aliphatic fat. The water signal showed less than 2% attenuation for all fat suppression configurations (data not shown).

The phantom's gel compartment showed monoexponential diffusion, with a measured  $\alpha = 1.00$  and  $K = 3.00$ ; its mean (SD)  $T_1$  and  $T_2$  were 1386.8 (19.2) ms and 46.6 (1.4) ms, respectively. All models yielded gel diffusion coefficients of  $1.90 \times 10^{-3} \text{ mm}^2/\text{s}$ , except IVIM, for which  $ADC = 1.87 \times 10^{-3} \text{ mm}^2/\text{s}$ ; IVIM showed the largest biases of the 4 models. Relative biases in each parameter were  $>8\%$  in fat-contaminated regions with no fat suppression or with SSGR (Fig. 5). For all models except IVIM, olefinic fat contamination produced a bias of 2-3%, irrespective of the fat suppression method used. Except for IVIM parameters, SPAIR reduced bias in all parameters below 8% in regions contaminated by aliphatic fat, while WSE+SPAIR+SSGR reduced it below 1%. WSE+SPAIR+SSGR and WSE+SPAIR gave similar parameter values, consistent with their comparable fat suppression performance. For coarsely-shimmed data, fat suppression performance was markedly poorer: no method produced biases

1  
2  
3 better than  $\pm 23\%$  in regions contaminated with aliphatic fat. Furthermore, SSGR and  
4  
5 WSE+SSGR showed large biases even in gel-only regions.  
6  
7  
8

## 9 **In Vivo Results**

10 **Quality of Fat Suppression In Vivo.** Example DWI images are shown in Fig. 6 for each fat  
11 suppression modality, along with mDIXON images. All fat suppression configurations showed  
12 pronounced shifted aliphatic fat signals, except WSE+SPAIR and WSE+SPAIR+SSGR. Of  
13 these, WSE+SPAIR+SSGR showed better fat suppression homogeneity, with shifted aliphatic fat  
14 being consistently suppressed across the field-of-view.  
15  
16  
17  
18

19 Fig. 7 highlights the increased bias in diffusion parameters in vivo as compared to in vitro.  
20 All diffusion coefficients showed similar, substantial biases in the presence of fat contamination.  
21 Derived values for  $K$ ,  $f_p$  and  $D^*$  tended to decrease with improved fat suppression, while  
22 estimated  $\alpha$  decreased. In muscle regions containing only intramuscular fat, biases were large  
23 with no fat suppression or with SSGR alone. In the younger participant, with BMI = 20, SPAIR  
24 reduced the absolute bias of parameters, except  $f_p$  and  $D^*$ , to  $<15\%$ , SPAIR+SSGR, WSE and  
25 WSE+SSGR all performed similarly, and WSE+SPAIR reduced biases below 10%. The same  
26 trends held true for data contaminated with shifted olefinic fat, where biases were similar to  
27 muscle data; however, IVIM showed larger biases than the other models. Finally, data  
28 contaminated with shifted aliphatic fat showed biases consistently around 20%, including with  
29 use of WSE+SPAIR and WSE+SSGR+SPAIR. This is likely due to structural differences in  
30 underlying muscle between the olefinic and aliphatic-fat-contaminated regions. In the older, BMI  
31 = 33 participant, parameter biases were generally greater due to reduced  $B_0$  homogeneity and a  
32 concomitant decrease in SNR; however, data obtained with WSE+SPAIR showed similarly low  
33 biases in both participants.  
34  
35  
36  
37  
38  
39  
40  
41  
42  
43  
44  
45  
46  
47

48 **In Vivo Normative Diffusion Parameters and Repeatability.** Diffusion parameters from in  
49 vivo hamstring muscle data are summarized in Table 1, along with goodness-of-fit and  
50 repeatability measures. Fig. 8 shows ROI-planning, maps for parameter visualization, and quality  
51 control images.  
52  
53  
54

55 In the hamstring muscles, the mean (SD) SNR in two participants was 39.7 (8.8). All  
56 models measured larger diffusion coefficients in the slice direction, parallel to muscle fibers,  
57  
58  
59  
60

1  
2  
3 than in the readout direction, perpendicular to fibers. In agreement with simulations and in vitro  
4 data, IVIM gave smaller diffusion coefficient estimates than the other models, all of which gave  
5 similar values. This disparity in diffusion coefficients was larger in vivo than in vitro; the mean  
6  
7 IVIM  $ADC$  was  $1.87 \times 10^{-3} \text{ mm}^2/\text{s}$  in the slice direction, while the other models' derived diffusion  
8 coefficients were  $\sim 2.13\text{--}2.17 \times 10^{-3} \text{ mm}^2/\text{s}$ .

9  
10 We measured  $\alpha \sim 1$  and  $K \sim 3$  parallel to muscle fibers, indicating near-monoexponential  
11 diffusion. Perpendicular to muscle fibers,  $\alpha$  and  $K$  tended toward non-Gaussian behavior, with  
12 mean (SD)  $\alpha = 0.94$  (0.04) and  $K = 3.27$  (0.13). The SX model also gave the best fit to the data,  
13 with a substantially smaller RMSE than other models.

14 Table 1 shows that diffusion coefficients were similarly repeatable for all models, with mean  
15 intra- and inter-session differences  $\leq 4\%$ , and lines of zero difference, indicating perfect  
16 correlation between scans, within the 95% limits of agreement. Estimates of  $\alpha$ ,  $K$ , and  $f_p'$  showed  
17 small mean differences, but  $K$  and  $f_p'$  had large limits of agreement: up to 0.34 difference from  
18 the mean for the former, and 5.8% absolute difference for the latter.  $D^*$  showed generally poor  
19 repeatability, with broad 95% limits of agreement and a line of zero difference typically close to  
20 or outside of those limits; Fig. 8 shows example  $D^*$  maps from repeat scans.

## 21 22 23 24 25 26 27 28 29 30 31 32 33 34 35 36 37 38 39 40 41 42 43 44 45 46 47 48 49 50 51 52 53 54 55 56 57 58 59 60

To our knowledge, this study is the first to investigate the effect of fat signals and fat suppression methodology on Gaussian and non-Gaussian diffusion parameter estimation in skeletal muscle, and it expands on earlier analyses of noise effects in such models (8-11). Previous work on fat in DWI focused on parameter bias arising from water signals, rather than lipid signals, in fat tissue (9, 13, 14). These works also used the diffusion tensor model, and are thus inherently low  $b$ -value, monoexponential studies. Our work considers only isotropic diffusion models, as non-Gaussian models have still seen little penetration into tensor formulations; however, extending this work to the tensor model would be a valuable next step.

We have demonstrated here that conventional and non-Gaussian models are sensitive to noise and shifted fat signals, as expected when performing any analysis in which sources of error are not adequately accounted for. We found that data quality can be improved by combining multiple fat suppression techniques with a high  $b$ -value acquisition and a baseline offset. Our

1  
2  
3 extensive simulations, discussed in the Supplementary Material, showed that different DWI  
4 fitting functions should be used depending on the experimental data. A baseline offset parameter  
5 (12) proves beneficial for ROI-based DWI fitting, where SNR is high and considerable fat  
6 signals can be present; our data show triple-fat-suppressed water-fat ratios of the order of 1–5%  
7 (data not shown) and SNRs of around 40, where it is appropriate to use an offset. Conversely,  
8 when applied in a low fat-fraction, low-to-middling SNR regime, the offset produces a small,  
9 positive parameter estimation bias. This effect can be mitigated by incorporating an additional  
10 noise parameter (8), which improves parameter estimation for middling SNR, low fat-fraction  
11 data. Finally, no offset or noise parameters are needed to fit data in the absence of lipid signals;  
12 however,  $b_{\max}$  must be chosen judiciously to avoid noise bias (6).  
13  
14  
15  
16  
17  
18  
19  
20

21 SX and kurtosis models require  $b$ -values up to  $5000 \text{ s/mm}^2$  to characterize signal persistence  
22 at high  $b$ -values (20, 25), which may be modeled in part by incorporation of an offset.  
23  
24

25 Monoexponential and IVIM models, however, are frequently applied with  $b_{\max}$  of  $1000 \text{ s/mm}^2$  or  
26 less, and are thus subject to large biases when fat is present. This could account for reported  
27 inconsistencies in muscle diffusion measures with aging (36). For example, Galbán et al.  
28 reported a reduction in calf muscle diffusion coefficients by up to 10% in older participants (5).  
29 By simulating Galbán's  $b$ -value scheme with muscle and lipid signals (Supplementary Material,  
30 Supp. Fig. 5), we observe a bias error in diffusion coefficient estimates of -10% upon addition of  
31 5% fat fraction. Increases in intramuscular fat content of this order have been demonstrated in  
32 aging (37), and should be carefully considered when interpreting diffusion coefficient changes.  
33  
34  
35  
36  
37  
38  
39  
40

41 In our corn oil and gel phantom, the commonly-used SPAIR fat suppression method was  
42 sufficient for accurate parameter estimation, even when the gel signal was contaminated with  
43 aliphatic fat. However, its effectiveness decreases with reduced  $B_0$  homogeneity, due to broad,  
44 hard-to-suppress fat resonances. This is clearly seen in the in vivo data presented here, where the  
45 use of SPAIR alone gave diffusion parameter estimates substantially different from those  
46 obtained with better-performing configurations. With a non-modeled baseline, representing a  
47 typical monoexponential or IVIM diffusion study, SPAIR-fat-suppressed data gave non-  
48 physiologic ADCs of  $0.7 \times 10^{-3} \text{ mm}^2/\text{s}$ , and showed bias errors around 20% for  $\alpha$  and  $K$  (data not  
49 shown). The smallest parameter bias was found for WSE+SPAIR and WSE+SPAIR+SSGR  
50 schemes, when models were applied with baseline offsets; WSE+SPAIR+SSGR reduced  
51  
52  
53  
54  
55  
56  
57

1  
2  
3 aliphatic fat signal to between 1 and 5% of the water signal in vivo, versus 10–30% for SPAIR  
4 alone (data not shown). Simulations showed that this was sufficient to estimate non-Gaussian  
5 diffusion parameters with a bias of less than 6%, for SNR = 40. In general, WSE+SPAIR and  
6  
7 WSE+SPAIR+SSGR performed similarly, though the latter gave slightly improved fat  
8 suppression homogeneity in vivo. These methods, and more-sophisticated approaches (18, 19),  
9 will prove useful when considerable intramuscular fat may be present, such as in the elderly, and  
10 in diseases such as type II diabetes.  
11  
12  
13  
14  
15

16 Olefinic fat was less well-suppressed than aliphatic fat in our experiments. While improved  
17 olefinic fat suppression has been achieved via multi-acquisition TE-shifting (18), navigated  
18 water-fat separation (19), or additional frequency-selective saturation pulses (13), these methods  
19 can be challenging to implement. We excluded shifted subcutaneous olefinic fat from our muscle  
20 ROIs, and no intramuscular olefinic fat signal was visible in our high  $b$ -value DWI or mDIXON  
21 images, consistent with previous work (18). With the further addition of a baseline offset to our  
22 model fits, we surmise that the effect of olefinic fat on our parameter estimates is minimal.  
23  
24  
25

26 With our triple-fat-suppressed DWI approach, in vivo diffusion coefficients showed  
27 minimal intra- and intersession differences; however, other parameters, particularly  $f_p$  and  $D^*$ ,  
28 showed broad 95% limits of agreement, with  $D^*$  showing the poorest repeatability overall. This  
29 is consistent with our simulations, and with previous work (22), confirming that  $D^*$  estimation is  
30 challenging at clinically-achievable SNRs. The poor repeatability of the IVIM model indicates  
31 that it may not be suitable for analysis of muscle microcirculation without further improvement.  
32  
33  
34  
35  
36  
37  
38  
39  
40

41 Skeletal muscle has complex architecture, comprising intra- and extra-cellular spaces, fat, and  
42 vasculature, and mobile protons are expected at a variety of displacement time and length scales.  
43 Thus, the “true” underlying signal behavior as a function of  $b$ -value may consist of  
44 superpositions or extensions of the functions investigated here. Indeed, the most commonly-used  
45 model, the monoexponential, is likely a substantial oversimplification of underlying signal  
46 behavior, while models such as SX and kurtosis have the potential for greater sensitivity and  
47 specificity to the details of muscle ultrastructure (20, 25). The present study represents the first  
48 application of the SX model to in vivo skeletal muscle diffusion data, with the derived values for  
49  $\alpha$  indicating the presence of non-Gaussian diffusion in the hamstring muscles.  
50  
51  
52  
53  
54  
55  
56  
57

1  
2  
3  
4  
5  
6  
7  
8  
9  
10  
11  
12  
13  
14  
15  
16  
17  
18  
19  
20  
21  
22  
23  
24  
25  
26  
27  
28  
29  
30  
31  
32  
33  
34  
35  
36  
37  
38  
39  
40  
41  
42  
43  
44  
45  
46  
47  
48  
49  
50  
51  
52  
53  
54  
55  
56  
57

Parallel to muscle fibers,  $\alpha$  was close to 1 in the majority of participants, suggesting that diffusion along fibers is monoexponential in these cases. However, there remains the possibility that these  $\alpha$  estimates are biased toward 1 by noise, as shown by our simulations. Furthermore, our DWI sequence may have too long a TE to detect  $\alpha$ -modifying short- $T_2$  components.

Perpendicular to muscle fibers, estimates of  $\alpha < 1$  suggested the presence of non-monoexponential signal decay in spite of possible noise bias. Several younger participants showed mean  $\alpha$  values around 0.9, indicating greater complexity perpendicular to muscle fibers than along fibers and representing an appreciable departure from the monoexponential case (38).

Consistent with our  $\alpha$  measurements, our  $K$  estimates also took non-monoexponential values, agreeing with Marschar et al. (6), who reported excess kurtosis between 0.1 and 0.4 in skeletal muscle. Both kurtosis and the SX are expected to highlight muscle tissue heterogeneity, reflecting multiple monoexponential diffusion components arising from intra- and extracellular compartments (20, 25), and different fiber types or dimensions (39). However, of the four models studied, the SX provided the best fit to the diffusion data, as shown by RMSE measures in Table 1. This suggests that the SX is the most appropriate of the models for characterizing muscle diffusion, but detailed model selection experiments are required to confirm this finding.

## CONCLUSION

Our extensive numerical simulations have shown that effective fat suppression is crucial for accurate measurement of diffusion parameters in skeletal muscle, and the commonly-used SPAIR fat suppression technique may be inadequate for this purpose. More thorough methods, such as triple-fat-suppressed DWI, are required for accurate and precise estimation of Gaussian and non-Gaussian diffusion parameters. Non-Gaussian parameters appear to give additional information on muscle microstructural properties beyond that provided by conventional models and, with further validation, they could be used to study muscle pathology and explore underlying causes of decline in muscle biomechanical quality with aging.

## ACKNOWLEDGEMENTS

We are grateful to Hasan Celik and Michael Schär, who graciously shared their expertise.

**REFERENCES**

1. Warach S, Chien D, Li W, Ronthal M, Edelman R. Fast magnetic resonance diffusion-weighted imaging of acute human stroke. *Neurology* 1992; 42: 1717-1723.
2. Sugahara T, Korogi Y, Kochi M, Ikushima I, Shigematu Y, Hirai T, Okuda T, Liang L, Ge Y, Komohara Y. Usefulness of diffusion-weighted MRI with echo-planar technique in the evaluation of cellularity in gliomas. *J Magn Reson Imaging* 1999; 9: 53-60.
3. Jensen JH, Helpert JA, Ramani A, Lu H, Kaczynski K. Diffusional kurtosis imaging: The quantification of non-gaussian water diffusion by means of magnetic resonance imaging. *Magn Reson Med* 2005; 53: 1432-1440.
4. Ababneh Z, Ababneh R, Maier S, Winalski C, Oshio K, Ababneh A, Mulkern R. On the correlation between T2 and tissue diffusion coefficients in exercised muscle: Quantitative measurements at 3T within the tibialis anterior. *Magn Reson Mater Phy* 2008; 21: 273-278.
5. Galbán CJ, Maderwald S, Stock F, Ladd ME. Age-related changes in skeletal muscle as detected by diffusion tensor magnetic resonance imaging. *J Gerontol A Biol Sci Med Sci* 2007; 62: 453-458.
6. Marschar AM, Kuder TA, Stieltjes B, Nagel AM, Bachert P, Laun FB. In vivo imaging of the time-dependent apparent diffusional kurtosis in the human calf muscle. *J Magn Reson Imaging* 2015; 41: 1581-1590.

- 1  
2  
3 7. Filli L, Kenkel D, Wurnig MC, Boss A. Diffusional kurtosis MRI of the lower leg:  
4  
5 changes caused by passive muscle elongation and shortening. *NMR Biomed* 2016; 29: 767-775.  
6  
7  
8  
9
- 10 8. Jones DK, Basser PJ. "Squashing peanuts and smashing pumpkins": How noise distorts  
11 diffusion-weighted MR data. *Magn Reson Med* 2004; 52: 979-993.  
12  
13
- 14 9. Damon BM. Effects of image noise in muscle diffusion tensor (DT)-MRI assessed  
15 using numerical simulations. *Magn Reson Med* 2008; 60: 934-944.  
16  
17  
18  
19  
20  
21  
22
- 23 10. Froeling M, Nederveen AJ, Nicolay K, Strijkers GJ. DTI of human skeletal muscle: the  
24 effects of diffusion encoding parameters, signal-to-noise ratio and T2 on tensor indices and  
25 fiber tracts. *NMR Biomed* 2013; 26: 1339-1352.  
26  
27  
28  
29  
30  
31
- 32 11. Kristoffersen A. Estimating non-Gaussian diffusion model parameters in the presence  
33 of physiological noise and Rician signal bias. *J Magn Reson Imaging* 2012; 35: 181-189.  
34  
35  
36  
37  
38
- 39 12. Hansmann J, Hernando D, Reeder SB. Fat confounds the observed apparent diffusion  
40 coefficient in patients with hepatic steatosis. *Magn Reson Med* 2013; 69: 545-552.  
41  
42  
43  
44
- 45 13. Williams SE, Heemskerk AM, Welch EB, Li K, Damon BM, Park JH. Quantitative  
46 effects of inclusion of fat on muscle diffusion tensor MRI measurements. *J Magn Reson Imaging*  
47 2013; 38: 1292-1297.  
48  
49  
50  
51  
52  
53  
54

- 1  
2  
3 14. Hooijmans M, Damon B, Froeling M, Versluis M, Burakiewicz J, Verschuuren J, Niks E,  
4  
5 Webb A, Kan H. Evaluation of skeletal muscle DTI in patients with duchenne muscular  
6  
7 dystrophy. *NMR Biomed* 2015; 28: 1589-1597.  
8  
9
- 10  
11 15. Rosen B, Wedeen V, Brady T. Selective saturation NMR imaging. *J Comput Assist*  
12  
13 *Tomogr* 1984; 8: 813-818.  
14  
15
- 16  
17 16. Meyer CH, Pauly JM, Macovski A, Nishimura DG. Simultaneous spatial and spectral  
18  
19 selective excitation. *Magn Reson Med* 1990; 15: 287-304.  
20  
21  
22
- 23  
24 17. Park H, Kim D, Cho Z. Gradient reversal technique and its applications to chemical-  
25  
26 shift-related NMR imaging. *Magn Reson Med* 1987; 4: 526-536.  
27  
28  
29
- 30  
31 18. Hernando D, Karampinos D, King K, Haldar J, Majumdar S, Georgiadis J, Liang ZP.  
32  
33 Removal of olefinic fat chemical shift artifact in diffusion MRI. *Magn Reson Med* 2011; 65:  
34  
35 692-701.  
36  
37  
38
- 39  
40 19. Burakiewicz J, Charles-Edwards GD, Goh V, Schaeffter T. Water-fat separation in  
41  
42 diffusion-weighted EPI using an IDEAL approach with image navigator. *Magn Reson Med*  
43  
44 2015; 73: 964-972.  
45  
46  
47
- 48  
49 20. Bennett KM, Schmainda KM, Rowe DB, Lu H, Hyde JS. Characterization of  
50  
51 continuously distributed cortical water diffusion rates with a stretched-exponential model.  
52  
53 *Magn Reson Med* 2003; 50: 727-734.  
54

- 1  
2  
3 21. Le Bihan D, Breton E, Lallemand D, Grenier P, Cabanis E, Laval-Jeantet M. MR  
4  
5 imaging of intravoxel incoherent motions: Application to diffusion and perfusion in neurologic  
6  
7 disorders. *Radiology* 1986; 161: 401-407.  
8  
9
- 10  
11 22. Lemke A, Laun FB, Simon D, Stieltjes B, Schad LR. An in vivo verification of the  
12  
13 intravoxel incoherent motion effect in diffusion-weighted imaging of the abdomen. *Magn*  
14  
15 *Reson Med* 2010; 64: 1580-1585.  
16  
17
- 18  
19 23. Stanisz GJ, Odobina EE, Pun J, Escaravage M, Graham SJ, Bronskill MJ, Henkelman  
20  
21 RM. T1, T2 relaxation and magnetization transfer in tissue at 3T. *Magn Reson Med* 2005; 54:  
22  
23 507-512.  
24  
25
- 26  
27 24. Bouhrara M, Reiter DA, Celik H, Bonny JM, Lukas V, Fishbein KW, Spencer RG.  
28  
29 Incorporation of Rician noise in the analysis of biexponential transverse relaxation in cartilage  
30  
31 using a multiple gradient echo sequence at 3 and 7 Tesla. *Magn Reson Med* 2015; 73: 352-366.  
32  
33  
34  
35  
36
- 37 25. Jensen JH, Helpert JA. MRI quantification of non-Gaussian water diffusion by kurtosis  
38  
39 analysis. *NMR Biomed* 2010; 23: 698-710.  
40  
41  
42  
43  
44
- 45 26. Freiman M, Voss SD, Mulkern RV, Perez-Rossello JM, Callahan MJ, Warfield SK. In  
46  
47 vivo assessment of optimal b-value range for perfusion-insensitive apparent diffusion coefficient  
48  
49 imaging. *Med Phys* 2012; 39: 4832-4839.  
50  
51
- 52 27. Cameron D, Bouhrara M, Reiter DA, Fishbein KW, Bergeron CM, Spencer RG.  
53  
54  
55  
56 Diffusion-weighted, triple-fat-suppressed echo-planar imaging provides 'anomalous' diffusion

1  
2  
3 metrics for assessment of muscle quality in the human thigh. Proc Intl Soc Mag Reson Med 23;  
4  
5 2015; Toronto, Canada. 4243.  
6  
7

8  
9  
10 28. Steidle G, Eibofner F, Schick F. Quantitative diffusion imaging of adipose tissue in the  
11 human lower leg at 1.5 T. Magn Reson Med 2011; 65: 1118-1124.  
12

13  
14  
15 29. Eggers H, Brendel B, Duijndam A, Herigault G. Dual-echo Dixon imaging with flexible  
16 choice of echo times. Magn Reson Med 2011; 65: 96-107.  
17  
18

19  
20  
21 30. Yu J, Agarwal H, Stuber M, Schär M. Practical signal-to-noise ratio quantification for  
22 sensitivity encoding: Application to coronary MR angiography. J Magn Reson Imaging 2011;  
23 33: 1330-1340.  
24  
25  
26  
27  
28

29  
30  
31 31. Vos SB, Tax CM, Luijten PR, Ourselin S, Leemans A, Froeling M. The importance of  
32 correcting for signal drift in diffusion MRI. Magn Reson Med 2017;DOI: 10.1002/mrm.26124.  
33  
34  
35

36  
37  
38 32. Tournier J-D, Mori S, Leemans A. Diffusion tensor imaging and beyond. Magn Reson  
39 Med 2011; 65: 1532-1556.  
40

41  
42  
43 33. Winfield JM, Douglas NHM, deSouza NM, Collins DJ. Phantom for assessment of fat  
44 suppression in large field-of-view diffusion-weighted magnetic resonance imaging. Phys Med  
45 Biol 2014; 59: 2235-2248.  
46  
47  
48

49  
50  
51 34. Lavdas I, Behan KC, Papadaki A, McRobbie DW, Aboagye EO. A phantom for  
52 diffusion-weighted MRI (DW-MRI). J Magn Reson Imaging 2013; 38: 173-179.  
53  
54  
55

- 1  
2  
3 35. Schär M, Kozerke S, Fischer SE, Boesiger P. Cardiac SSFP imaging at 3 Tesla. *Magn Reson Med* 2004; 51: 799-806.  
4  
5  
6  
7  
8  
9
- 10 36. Oudeman J, Nederveen AJ, Strijkers GJ, Maas M, Luijten PR, Froeling M. Techniques  
11 and applications of skeletal muscle diffusion tensor imaging: A review. *J Magn Reson Imaging*  
12 2015; 43: 773-788.  
13  
14  
15  
16  
17  
18 37. Marcus R, Addison O, Kidde J, Dibble L, Lastayo P. Skeletal muscle fat infiltration:  
19 Impact of age, inactivity, and exercise. *J Nutr Health Aging* 2010; 14: 362-366.  
20  
21  
22  
23  
24 38. Johnston D. Stretched exponential relaxation arising from a continuous sum of  
25 exponential decays. *Physical Review B* 2006; 74: 184430.  
26  
27  
28  
29  
30 39. Schiaffino S, Reggiani C. Fiber types in mammalian skeletal muscles. *Physiol Rev* 2011;  
31 91: 1447-1531.  
32  
33  
34  
35  
36  
37  
38  
39  
40  
41  
42  
43  
44  
45  
46  
47  
48  
49  
50  
51  
52  
53  
54  
55

SLICE (n = 10)							
Model	$D$ or $D^*$ ( $\text{mm}^2/\text{s}$ )	MD <sub>intra</sub> (95% LA)	MD <sub>inter</sub> (95% LA)	Parameters	MD <sub>intra</sub> (95% LA)	MD <sub>inter</sub> (95% LA)	RMSE
<b>Mono</b>	2.13 (0.12) $\times 10^{-3}$	-0.03 (-0.19, 0.12) $\times 10^{-3}$	-0.06 (-0.33, 0.20) $\times 10^{-3}$	—	—	—	7.2 (3.7)
<b>IVIM</b>	30.4 (37.7) $\times 10^{-3}$	11.8 (-135, 111) $\times 10^{-3}$	59.6 (-25, 145) $\times 10^{-3}$	$f_p' = 3.3$ (1.9) %	0.3 (-5.1, 5.8) %	1.1 (-1.1, 3.2) %	14.3 (6.4)
<b>---Perf.</b>	1.87 (0.08) $\times 10^{-3}$	-0.01 (-0.06, 0.09) $\times 10^{-3}$	-0.02 (-0.18, 0.14) $\times 10^{-3}$	$f_d' = 96.7$ (1.9) %	-0.3 (-5.8, 5.1) %	-1.1 (-3.2, 1.1) %	(6.4)
<b>---Diff.</b>	2.14 (0.13) $\times 10^{-3}$	-0.04 (-0.23, 0.14) $\times 10^{-3}$	-0.08 (-0.39, 0.23) $\times 10^{-3}$	$\alpha = 0.97$ (0.03)	0.02 (-0.05, 0.09)	0.02 (-0.07, 0.11)	5.2 (3.9)
<b>---Kurtosis</b>	2.17 (0.15) $\times 10^{-3}$	-0.05 (-0.30, 0.19) $\times 10^{-3}$	-0.08 (-0.45, 0.29) $\times 10^{-3}$	$K = 3.09$ (0.11)	-0.06 (-0.30, 0.18)	-0.03 (-0.32, 0.26)	5.5 (3.3)
READ (n = 8)							
Model	$D$ or $D^*$ ( $\text{mm}^2/\text{s}$ )	MD <sub>intra</sub> (95% LA)	MD <sub>inter</sub> (95% LA)	Parameters	MD <sub>intra</sub> (95% LA)	MD <sub>inter</sub> (95% LA)	RMSE
<b>Mono</b>	1.43 (0.06) $\times 10^{-3}$	0.04 (-0.05, 0.12) $\times 10^{-3}$	0.02 (-0.16, 0.20) $\times 10^{-3}$	—	—	—	19.8 (11.2)
<b>IVIM</b>	9.04 (7.57) $\times 10^{-3}$	-4.5 (-26.5, 17.6) $\times 10^{-3}$	4.7 (-11.1, 20.6) $\times 10^{-3}$	$f_p' = 2.5$ (1.3) %	0.3 (-1.7, 1.0) %	0.6 (-2.2, 3.4) %	17.9 (7.0)
<b>---Perf.</b>	1.23 (0.05) $\times 10^{-3}$	0.01 (-0.06, 0.09) $\times 10^{-3}$	-0.05 (-0.23, 0.12) $\times 10^{-3}$	$f_d' = 97.5$ (1.3) %	-0.3 (-2.4, 1.8) %	-0.6 (-3.4, 2.2) %	(7.0)
<b>---Diff.</b>	1.43 (0.05) $\times 10^{-3}$	0.05 (-0.10, 0.20) $\times 10^{-3}$	0 (-0.17, 0.17) $\times 10^{-3}$	$\alpha = 0.94$ (0.04)	-0.02 (-0.13, 0.09)	-0.05 (-0.14, 0.03)	9.9 (6.2)
<b>---Kurtosis</b>	1.47 (0.06) $\times 10^{-3}$	0.08 (-0.09, 0.18) $\times 10^{-3}$	0.01 (-0.16, 0.19) $\times 10^{-3}$	$K = 3.27$ (0.13)	0.03 (-0.25, 0.30)	0 (-0.34, 0.34)	11.8 (6.6)

**Table 1. Calculated in vivo diffusion parameters and their repeatability.** Results are shown for ROIs drawn in the hamstring muscles (see Figure 9). Data are obtained from triple fat-suppressed images with diffusion-sensitization in the slice-select (parallel to muscle fibers) and readout (perpendicular to muscle fibers) directions. Measurements are quoted as mean (SD) over all participants. Intra- and inter-session repeatability are described in 5 participants by Bland-Altman measures: namely, mean difference (MD), and 95% limits of agreement (LA) in brackets.  $D$  = diffusion coefficient, including the apparent diffusion coefficient (monoexponential and IVIM models) and the distributed diffusion coefficient (stretched exponential and kurtosis models),  $D^*$  = pseudo-diffusion coefficient,  $f_p'$  = corrected perfusion fraction,  $f_d'$  = corrected diffusion fraction,  $\alpha$  = stretching parameter, IVIM = intravoxel incoherent motion,  $K$  = kurtosis.

**Figure 1: Pulse sequence diagram showing the triple-fat-suppressed, diffusion-weighted spin echo single-shot echo-planar imaging (EPI) sequence used in this study.** This consists of a diffusion-weighted spin echo sequence with a ramp-sampling EPI readout, preceded by a spectral attenuated inversion recovery (SPAIR) module, which suppresses fat via an adiabatic inversion pulse followed by gradient spoilers (Sp). The SPAIR TI used in this study was 200 ms, and the TE was 71 ms. Further fat suppression was achieved using water-specific excitation (WSE, highlighted in green) and slice-select gradient reversal (SSGR, highlighted in blue) within the spin echo sequence. WSE consisted of a slice-selective composite RF pulse in a 1–4–6–4–1 configuration, with interpulse intervals of 1.15 ms, and component flip angles of  $5.6^\circ$ – $22.5^\circ$ – $33.8^\circ$ – $22.5^\circ$ – $5.6^\circ$ , adding to the equivalent of a  $90^\circ$  excitation. SSGR consisted of a reversal of the slice-select gradient polarity during the spin echo refocusing pulse. Note that  $G_z$  = slice-select direction,  $G_y$  = phase encoding direction, and  $G_x$  = readout direction, and diffusion-weighted (DW) gradients are shown as dashed blocks. Gradients were played along only a single axis for each implementation of the sequence, depending on the desired direction of diffusion sensitization.

**Figure 2: Plots of bias and dispersion in fitted parameters for all four candidate diffusion models in Monte-Carlo simulations.** Results are visualized as colored matrix plots, grouped by monoexponential, stretched exponential, kurtosis, and intravoxel incoherent motion (IVIM) models. These are subdivided into their fitted parameters by dashed lines, where top and bottom rows denote relative bias (B%) and relative dispersion (D%), respectively. Columns denote different input parameter values, as obtained from the in vivo literature (non-monoexponential diffusion coefficients and the IVIM pseudo-diffusion coefficient,  $D^*$ , were fixed at  $2.0 \times 10^{-3} \text{ mm}^2/\text{s}$  and  $25 \times 10^{-3} \text{ mm}^2/\text{s}$ , respectively). Individual matrix plots are shown with signal-to-noise ratios (SNRs) increasing along the x-axis (1–50 in increments of 0.25), with a separate column for infinite SNR; fat signal fractions are shown on the y-axis, (0–25% in increments of 0.125%). The color lookup table of relative bias and dispersion was limited to  $\pm 75\%$  to improve color contrast between different model parameters. As shown, for most diffusion coefficient estimates parameter bias and dispersion tend to increase as SNR decreases, and a subtle bias is seen for small fat fractions. For IVIM, ADC bias increases strongly with inlarge, discrete biases were seen in the perfusion fraction,  $f_p$ , where fat signal adds to the apparent slow-diffusing fraction

1  
2  
3 while simultaneously skewing the fit of  $f_p$  toward larger values.  $ADC$  = apparent diffusion  
4 coefficient,  $\alpha$  = stretching parameter,  $DDC$  = distributed diffusion coefficient, and  $K$  = kurtosis.  
5  
6  
7  
8

9 **Figure 3: Phantom fat suppression results and example parameter maps.** The top two rows  
10 show multiecho two-point Dixon (mDIXON) water and fat images (top left), diffusion-weighted  
11  $b = 1380 \text{ s/mm}^2$  images for all 8 fat suppression combinations, and positioning of the regions of  
12 interest (ROIs) within the phantom. In these images, olefinic fat signal is shifted up slightly,  
13 while aliphatic fat signal is shifted down to a much greater degree, due to its large chemical shift  
14 relative to water. A diagram of the phantom is shown in the bottom left, and some example  
15 parameter maps from all four diffusion models are shown in the bottom two rows of the figure.  
16 The third row shows maps generated from the non-fat-suppressed diffusion-weighted images  
17 (left-hand arrow), and the fourth row shows maps from data obtained with a combination of  
18 water-specific excitation (WSE), spectral attenuated inversion recovery (SPAIR), and slice select  
19 gradient reversal (SSGR) fat suppression methods (right-hand arrow). Images were acquired in  
20 the axial plane with diffusion sensitization in the slice direction. ROIs were defined in shifted  
21 olefinic fat (pale blue) and aliphatic fat (pale green) alone, for calculation of water-fat signal  
22 ratios (Fig. 4), and in gel contaminated with olefinic fat (dark blue) and aliphatic fat (green), to  
23 evaluate the effect of fat contamination on parameter estimation (Fig. 5). Uncontaminated  
24 agarose gel (red) is used as a reference for both of these analyses. As shown, shifted aliphatic fat  
25 signals are prominent for all fat suppression configurations except WSE+SPAIR and  
26 WSE+SPAIR+SSGR, leading to parameter estimation bias in the example maps, while shifted  
27 olefinic fat remains in all cases.  $ADC$  = apparent diffusion coefficient,  $\alpha$  = stretching parameter,  
28  $DDC$  = distributed diffusion coefficient,  $f_p$  = perfusion fraction, IVIM = intravoxel incoherent  
29 motion, and  $K$  = kurtosis.  
30  
31  
32  
33  
34  
35  
36  
37  
38  
39  
40  
41  
42  
43  
44  
45  
46  
47

48 **Figure 4: Water-fat signal ratios obtained from phantom images using combinations of fat**  
49 **suppression methods.** Measurements were made on  $b = 1000 \text{ s/mm}^2$  diffusion-weighted images,  
50 where water and fat signals were clearly visible, using the red, pale green, and pale blue ROIs  
51 shown in Fig. 3. Signal intensities were measured in shifted fat and agarose gel for each fat  
52 suppression combination, and are expressed as mean water:olefinic-fat and water:aliphatic-fat  
53 ratios in the bar plot shown. All fat suppression combinations were applied in series and repeated  
54  
55  
56  
57  
58  
59  
60

1  
2  
3 in five separate scan sessions, with the phantom being removed, recentered and reshimmed  
4 between sessions; error bars show the standard deviations of water-fat ratios across each of the  
5 five acquisitions. As shown, water:aliphatic-fat was largest for WSE+SPAIR+SSGR and  
6 marginally smaller for WSE+SPAIR. Water:olefinic-fat was relatively constant in all cases,  
7 indicating the difficulty in suppressing olefinic fat along with aliphatic fat. SSGR = slice select  
8 gradient reversal, SPAIR = spectral attenuated inversion recovery, WSE = water-specific  
9 excitation.  
10  
11  
12  
13  
14  
15  
16  
17

18 **Figure 5: Comparison of in vitro diffusion parameter estimates using different fat**  
19 **suppression combinations.** Results are shown for diffusion sensitization in the slice-select  
20 direction; ‘Shim 1’ and Shim 2’ represent data acquired with a projection-based shim, with SNR  
21 = 110, and a coarse, image-based shim, with SNR = 41, respectively. Each shim was applied  
22 across the whole phantom. Data are shown for gel contaminated by shifted aliphatic fat (left-  
23 hand column, A), gel contaminated by shifted olefinic fat (middle column, O), and gel alone  
24 (right-hand column, G); namely, from the green, dark blue, and red ROIs illustrated in Fig. 3.  
25 Gel-only parameter values obtained from well-shimmed, non-fat-suppressed data were taken as  
26 the reference values, and thus the top-right cell of each ‘Shim 1’ plot has an error of 0%. These  
27 reference values were chosen to represent pure gel parameters without possible signal  
28 perturbation effects from the fat suppression methods. It can be seen that parameter biases tend  
29 toward zero as fat suppression methods are added, but this trend is weakened when  $B_0$  shimming  
30 is poor.  $ADC$  = apparent diffusion coefficient,  $\alpha$  = stretching parameter,  $D^*$  = pseudo-diffusion  
31 coefficient,  $DDC$  = distributed diffusion coefficient,  $f_p$  = perfusion fraction, IVIM = intravoxel  
32 incoherent motion,  $K$  = kurtosis, SSGR = slice select gradient reversal, SPAIR = spectral  
33 attenuated inversion recovery, WSE = water-specific excitation.  
34  
35  
36  
37  
38  
39  
40  
41  
42  
43  
44  
45  
46  
47

48 **Figure 6: In vivo fat suppression results.** Representative multiecho two-point Dixon  
49 (mDIXON) water and fat images, in vivo region of interest (ROI) positioning, and diffusion-  
50 weighted,  $b = 1380 \text{ s/mm}^2$  images for all 8 fat suppression configurations are shown. As in Fig.  
51 3, olefinic fat signal is shifted up, overlapping muscle signal at the posterior of the thigh, while  
52 aliphatic fat signal is shifted down to a greater degree, obscuring muscle across the femur and  
53 part of the quadriceps femoris. Images were acquired axially across the thigh, with diffusion  
54  
55  
56  
57

1  
2  
3 sensitization in the slice direction, corresponding to the long axes of muscle fibers. ROIs (upper  
4 right image) were defined in muscle contaminated by shifted olefinic fat (dark blue), muscle  
5 contaminated by shifted aliphatic fat (green), and uncontaminated hamstring muscles (red) to  
6  
7 evaluate the effect of fat contamination on model parameter estimation (Fig. 7). As shown,  
8 pronounced shifted aliphatic fat signals are present for all fat suppression configurations, except  
9 WSE+SPAIR and WSE+SPAIR+SSGR. SPAIR = spectral attenuated inversion recovery, SSGR  
10 = slice select gradient reversal, WSE = water-specific excitation.  
11  
12  
13  
14  
15  
16  
17

18 **Figure 7. Comparison of in vivo diffusion parameter estimates using different fat**  
19 **suppression combinations.** Results were obtained from two healthy volunteers: both male, ages  
20 30 and 51 years, BMI = 20 and 33, and SNR = 83 and 45, respectively. Diffusion sensitization  
21 was applied in the slice-select direction, corresponding to the long axes of muscle fibers, and the  
22 readout direction, corresponding to their short axes. Plots show data from the green, dark blue,  
23 and red ROIs illustrated in Fig. 6: muscle and shifted aliphatic fat (left-hand column, A), muscle  
24 and shifted olefinic fat (middle column, O), and muscle alone (right-hand column, M). The color  
25 scale shows the relative bias with respect to triple-fat-suppressed muscle; therefore, the bottom-  
26 right cell of each plot has an error of 0%. Note that these reference values are different from  
27 those of Fig. 5, and ROIs are planned in different muscle regions with possible structural  
28 differences. In this case, the muscle signals contain contributions from intramuscular fat, and  
29 thus the best measure of pure muscle parameters is obtained when all 3 fat suppression methods  
30 are applied together. Parameter biases appear large in muscle, even where there is no visible fat  
31 signal; however, the addition of fat suppression methods eliminates this contribution and pushes  
32 parameter biases toward zero. The older participant, with higher BMI, shows larger parameter  
33 biases in general, but these are sufficiently reduced by the most effective fat suppression  
34 combinations.  $ADC$  = apparent diffusion coefficient,  $\alpha$  = stretching parameter,  $DDC$  =  
35 distributed diffusion coefficient,  $f_p$  = perfusion fraction,  $IVIM$  = intravoxel incoherent motion,  $K$   
36 = kurtosis,  $SSGR$  = slice select gradient reversal,  $SPAIR$  = spectral attenuated inversion  
37 recovery,  $WSE$  = water-specific excitation.  
38  
39  
40  
41  
42  
43  
44  
45  
46  
47  
48  
49  
50  
51  
52  
53  
54

55 **Figure 8: Diffusion parameter maps and region-of-interest (ROI) positioning.** Parameter  
56 maps were generated from data with a signal-to-noise ratio (SNR) of 45, and are organized by  
57

1  
2  
3 model and diffusion sensitization direction. The following b-values were used: 0, 276, 381, 525,  
4 725, 1000, 1380, 1904, 2627, 3624, and 5000 s/mm<sup>2</sup> for monoexponential, stretched exponential,  
5 and kurtosis models; and 0, 10, 18, 33, 60, 110, 276, 381, 525, 725, and 1000 s/mm<sup>2</sup> for  
6 intravoxel incoherent motion (IVIM). IVIM was fit with constraints on the perfusion fraction,  $f_p$ ,  
7 and the pseudo-diffusion coefficient,  $D^*$  (0–50% and  $5–150 \times 10^{-3}$  mm<sup>2</sup>/s, respectively); when  
8 parameters converged to these limits, the corresponding pixel was excluded from the map.  
9 ‘Repeat Scans’ highlight variation in  $D^*$  in a second scan session. ‘ROI Positioning’ shows an  
10 example of a region of interest, highlighted in purple, used to calculate the parameter values  
11 listed in Table 1. ‘Quality Control’ figures were used as a guide for ROI definition and to check  
12 for intramuscular fat. These include root-mean-square error (RMSE) and baseline offset (bsl)  
13 maps, both in signal units, generated from a monoexponential fit with diffusion sensitization in  
14 the slice direction; a water/fat image for masking residual fat (a  $b = 5000$  s/mm<sup>2</sup> image, purple,  
15 overlaid on an mDIXON water image, green); and an mDIXON fat image. Also shown are  $b = 0$   
16 and noise images used to calculate SNR.  $ADC$  = apparent diffusion coefficient,  $DDC$  =  
17 distributed diffusion coefficient,  $\alpha$  = stretching parameter, and  $K$  = kurtosis.  
18  
19  
20  
21  
22  
23  
24  
25  
26  
27  
28  
29  
30  
31  
32  
33  
34  
35  
36  
37  
38  
39  
40  
41  
42  
43  
44  
45  
46  
47  
48  
49  
50  
51  
52  
53  
54  
55  
56  
57

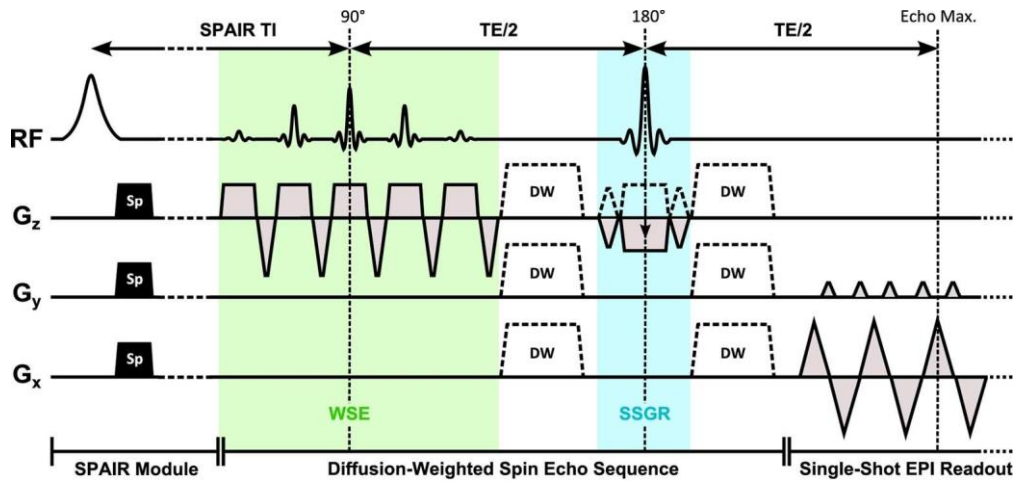


Figure 1: Pulse sequence diagram showing the triple-fat-suppressed, diffusion-weighted spin echo single-shot echo-planar imaging (EPI) sequence used in this study. This consists of a diffusion-weighted spin echo sequence with a ramp-sampling EPI readout, preceded by a spectral attenuated inversion recovery (SPAIR) module, which suppresses fat via an adiabatic inversion pulse followed by gradient spoilers (Sp). The SPAIR TI used in this study was 200 ms, and the TE was 71 ms. Further fat suppression was achieved using water-specific excitation (WSE, highlighted in green) and slice-select gradient reversal (SSGR, highlighted in blue) within the spin echo sequence. WSE consisted of a slice-selective composite RF pulse in a 1-4-6-4-1 configuration, with interpulse intervals of 1.15 ms, and component flip angles of 5.6°-22.5°-33.8°-22.5°-5.6°, adding to the equivalent of a 90° excitation. SSGR consisted of a reversal of the slice-select gradient polarity during the spin echo refocusing pulse. Note that  $G_z$  = slice-select direction,  $G_y$  = phase encoding direction, and  $G_x$  = readout direction, and diffusion-weighted (DW) gradients are shown as dashed blocks. Gradients were played along only a single axis for each implementation of the sequence, depending on the desired direction of diffusion sensitization.

Fig. 1

146x68mm (300 x 300 DPI)

1  
2  
3  
4  
5  
6  
7  
8  
9  
10  
11  
12  
13  
14  
15  
16  
17  
18  
19  
20  
21  
22  
23  
24  
25  
26  
27  
28  
29  
30  
31  
32  
33  
34  
35  
36  
37  
38  
39  
40  
41  
42  
43  
44  
45  
46  
47  
48  
49  
50  
51  
52  
53  
54  
55  
56  
57  
58  
59  
60

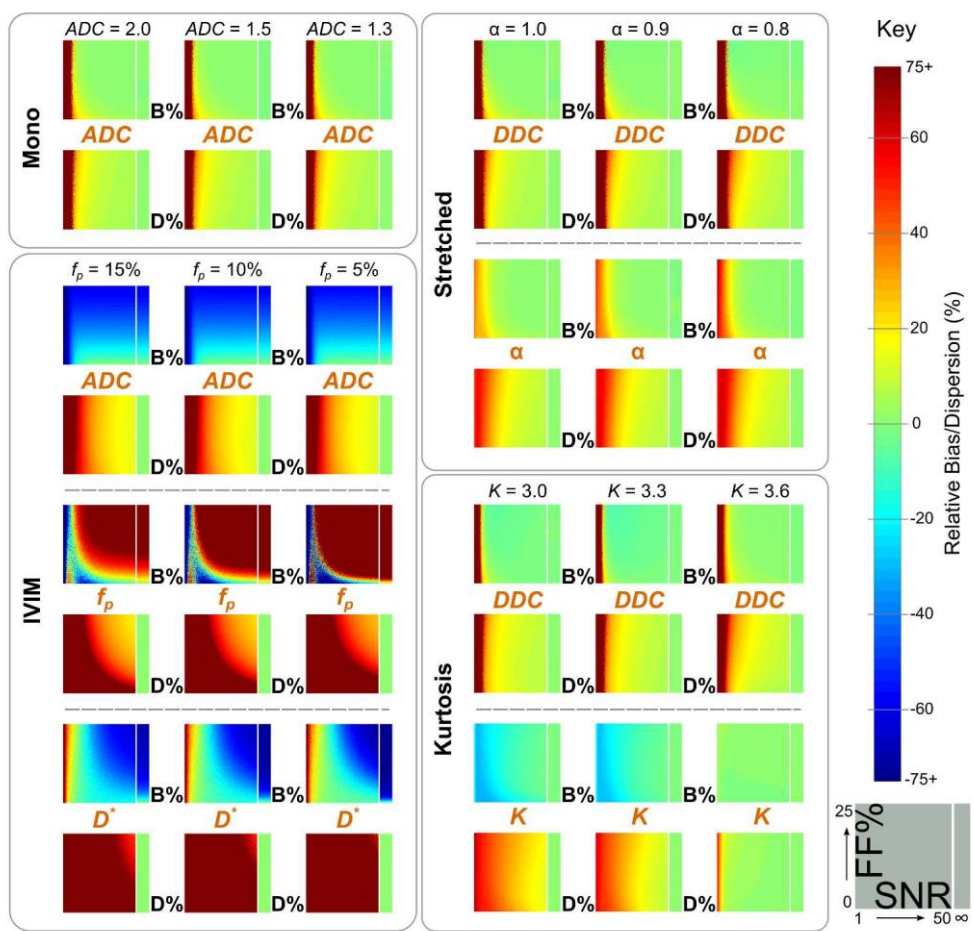


Figure 2: Plots of bias and dispersion in fitted parameters for all four candidate diffusion models in Monte-Carlo simulations. Results are visualized as colored matrix plots, grouped by monoexponential, stretched exponential, kurtosis, and intravoxel incoherent motion (IVIM) models. These are subdivided into their fitted parameters by dashed lines, where top and bottom rows denote relative bias (B%) and relative dispersion (D%), respectively. Columns denote different input parameter values, as obtained from the in vivo literature (non-monoexponential diffusion coefficients and the IVIM pseudo-diffusion coefficient,  $D^*$ , were fixed at  $2.0 \times 10^{-3} \text{ mm}^2/\text{s}$  and  $25 \times 10^{-3} \text{ mm}^2/\text{s}$ , respectively). Individual matrix plots are shown with signal-to-noise ratios (SNRs) increasing along the x-axis (1–50 in increments of 0.25), with a separate column for infinite SNR; fat signal fractions are shown on the y-axis, (0–25% in increments of 0.125%). The color lookup table of relative bias and dispersion was limited to  $\pm 75\%$  to improve color contrast between different model parameters. As shown, for most diffusion coefficient estimates parameter bias and dispersion tend to increase as SNR decreases, and a subtle bias is seen for small fat fractions. For IVIM, ADC bias increases strongly with inlarge, discrete biases were seen in the perfusion fraction,  $f_p$ , where fat signal adds to the apparent slow-diffusing fraction while simultaneously skewing the fit of  $f_p$  toward larger values. ADC = apparent diffusion coefficient,  $\alpha$  = stretching parameter, DDC = distributed diffusion coefficient, and  $K$  = kurtosis.

Fig. 2

304x289mm (300 x 300 DPI)

1  
2  
3  
4  
5  
6  
7  
8  
9  
10  
11  
12  
13  
14  
15  
16  
17  
18  
19  
20  
21  
22  
23  
24  
25  
26  
27  
28  
29  
30  
31  
32  
33  
34  
35  
36  
37  
38  
39  
40  
41  
42  
43  
44  
45  
46  
47  
48  
49  
50  
51  
52  
53  
54  
55  
56  
57  
58  
59  
60

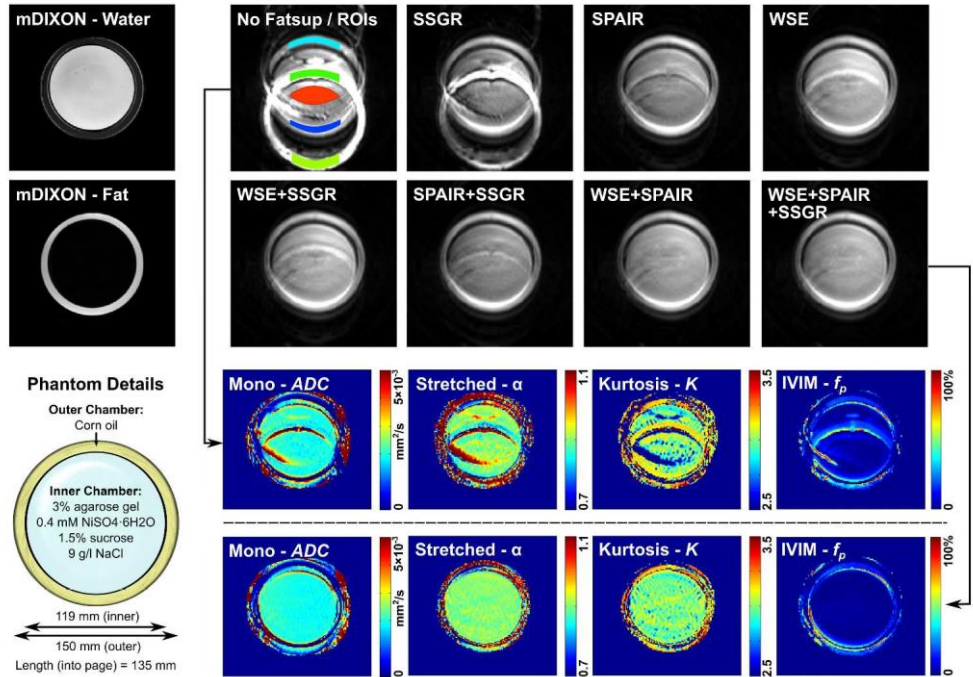


Figure 3: Phantom fat suppression results and example parameter maps. The top two rows show modified DIXON (mDIXON) water and fat images (top left), diffusion-weighted  $b = 1380 \text{ s/mm}^2$  images for all 8 fat suppression combinations, and positioning of the region of interest (ROI) within the phantom. In these images, olefinic fat signal is shifted up slightly, while aliphatic fat signal is shifted down to a much greater degree, due to its large chemical shift relative to water. A diagram of the phantom is shown in the bottom left, and some example parameter maps from all four diffusion models are shown in the bottom two rows of the figure. The third row shows maps generated from the non-fat-suppressed diffusion-weighted images (left-hand arrow), and the fourth row shows maps from data obtained with a combination of water-specific excitation (WSE), spectral attenuated inversion recovery (SPAIR), and slice select gradient reversal (SSGR) fat suppression methods (right-hand arrow). Images were acquired in the axial plane with diffusion sensitization in the slice direction. ROIs were defined in shifted olefinic fat (pale blue) and aliphatic fat (pale green) alone, for calculation of water-fat signal ratios (Fig. 4), and in gel contaminated with olefinic fat (dark blue) and aliphatic fat (green), to evaluate the effect of fat contamination on parameter estimation (Fig. 5). Uncontaminated agarose gel (red) is used as a reference for both of these analyses. As shown, shifted aliphatic fat signals are prominent for all fat suppression configurations except WSE+SPAIR and WSE+SPAIR+SSGR, leading to parameter estimation bias in the example maps, while shifted olefinic fat remains in all cases. ADC = apparent diffusion coefficient,  $\alpha$  = stretching parameter, DDC = distributed diffusion coefficient,  $f_p$  = perfusion fraction, IVIM = intravoxel incoherent motion, and  $K$  = kurtosis.

Fig. 3  
451x310mm (300 x 300 DPI)

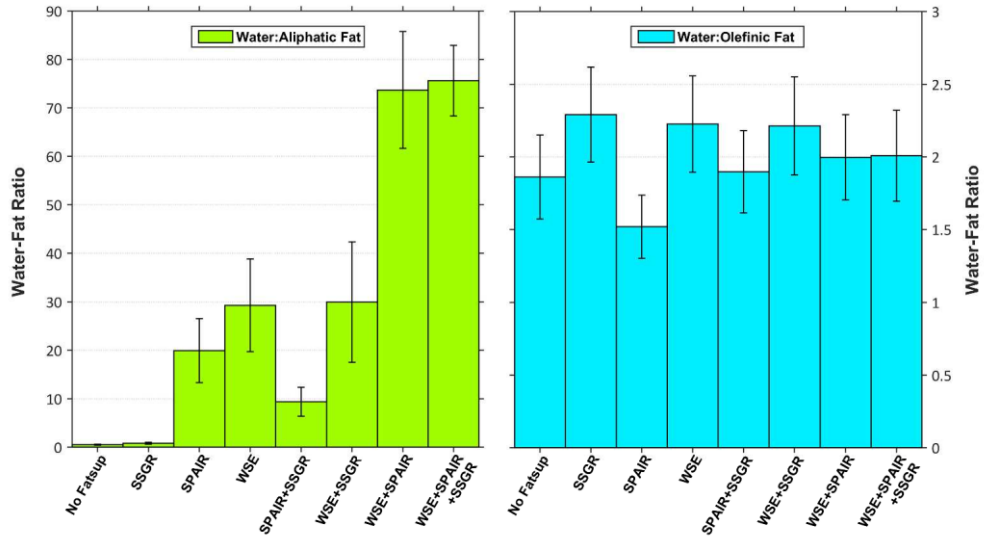


Figure 4: Water-fat signal ratios obtained from phantom images using combinations of fat suppression methods. Measurements were made on  $b = 1000 \text{ s/mm}^2$  diffusion-weighted images, where water and fat signals were clearly visible, using the red, pale green, and pale blue ROIs shown in Fig. 3. Signal intensities were measured in shifted fat and agarose gel for each fat suppression combination, and are expressed as mean water:olefinic-fat and water:aliphatic-fat ratios in the bar plot shown. All fat suppression combinations were applied in series and repeated in five separate scan sessions, with the phantom being removed, recentered and reshimmed between sessions; error bars show the standard deviations of water-fat ratios across each of the five acquisitions. As shown, water:aliphatic-fat was largest for WSE+SP-PAIR+SSGR and marginally smaller for WSE+SP-PAIR. Water:olefinic-fat was relatively constant in all cases, indicating the difficulty in suppressing olefinic fat along with aliphatic fat. SSGR = slice select gradient reversal, SP-PAIR = spectral attenuated inversion recovery, WSE = water-specific excitation.

Fig. 4

309x170mm (300 x 300 DPI)

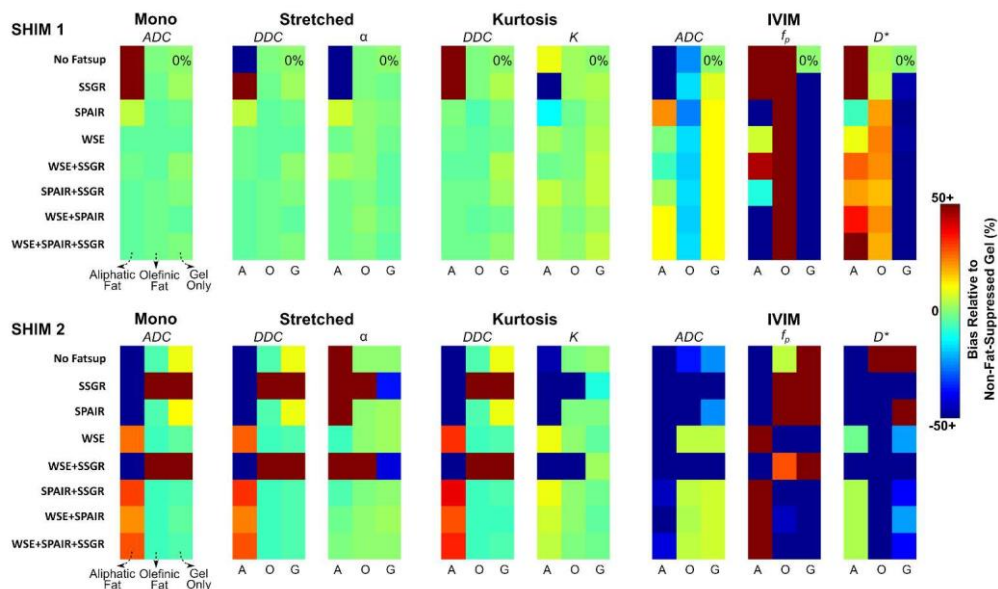


Figure 5: Comparison of in vitro diffusion parameter estimates using different fat suppression combinations. Results are shown for diffusion sensitization in the slice-select direction; 'Shim 1' and Shim 2' represent data acquired with a projection-based shim, with SNR = 110, and a coarse, image-based shim, with SNR = 41, respectively. Each shim was applied across the whole phantom. Data are shown for gel contaminated by shifted aliphatic fat (left-hand column, A), gel contaminated by shifted olefinic fat (middle column, O), and gel alone (right-hand column, G); namely, from the green, dark blue, and red ROIs illustrated in Fig. 3. Gel-only parameter values obtained from well-shimmed, non-fat-suppressed data were taken as the reference values, and thus the top-right cell of each 'Shim 1' plot has an error of 0%. These reference values were chosen to represent pure gel parameters without possible signal perturbation effects from the fat suppression methods. It can be seen that parameter biases tend toward zero as fat suppression methods are added, but this trend is weakened when  $B_0$  shimming is poor. ADC = apparent diffusion coefficient,  $\alpha$  = stretching parameter,  $D^*$  = pseudo-diffusion coefficient, DDC = distributed diffusion coefficient,  $f_p$  = perfusion fraction, IVIM = intravoxel incoherent motion, K = kurtosis, SSGR = slice select gradient reversal, SPAIR = spectral attenuated inversion recovery, WSE = water-specific excitation.

Fig. 5

421x254mm (299 x 299 DPI)

1  
2  
3  
4  
5  
6  
7  
8  
9  
10  
11  
12  
13  
14  
15  
16  
17  
18  
19  
20  
21  
22  
23  
24  
25  
26  
27  
28  
29  
30  
31  
32  
33  
34  
35  
36  
37  
38  
39  
40  
41  
42  
43  
44

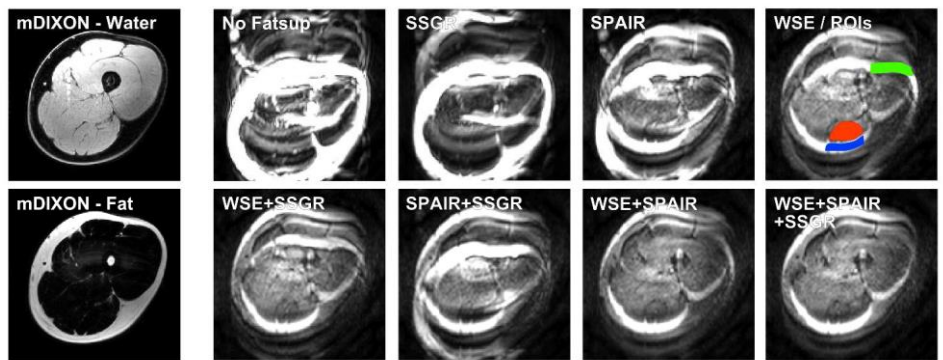


Figure 6: In vivo fat suppression results. Representative modified DIXON (mDIXON) water and fat images, in vivo region of interest (ROI) positioning, and diffusion-weighted,  $b = 1380 \text{ s/mm}^2$  images for all 8 fat suppression configurations are shown. As in Fig. 3, olefinic fat signal is shifted up, overlapping muscle signal at the posterior of the thigh, while aliphatic fat signal is shifted down to a greater degree, obscuring muscle across the femur and part of the quadriceps femoris. Images were acquired axially across the thigh, with diffusion sensitization in the slice direction, corresponding to the long axes of muscle fibers. ROIs (upper right image) were defined to evaluate the effect of fat contamination on model parameter estimation (Fig. 7), and are positioned in muscle contaminated by shifted olefinic fat (dark blue), muscle contaminated by shifted aliphatic fat (green), and in uncontaminated hamstring muscles (red). As shown, pronounced shifted aliphatic fat signals are present for all fat suppression configurations, except WSE+SPAIR and WSE+SPAIR+SSGR. SPAIR = spectral attenuated inversion recovery, SSGR = slice select gradient reversal, WSE = water-specific excitation.

Fig. 6  
438x169mm (299 x 299 DPI)

1  
2  
3  
4  
5  
6  
7  
8  
9  
10  
11  
12  
13  
14  
15  
16  
17  
18  
19  
20  
21  
22  
23  
24  
25  
26  
27  
28  
29  
30  
31  
32  
33  
34  
35  
36  
37  
38  
39  
40  
41  
42  
43  
44  
45  
46  
47  
48  
49  
50  
51  
52  
53  
54  
55  
56  
57

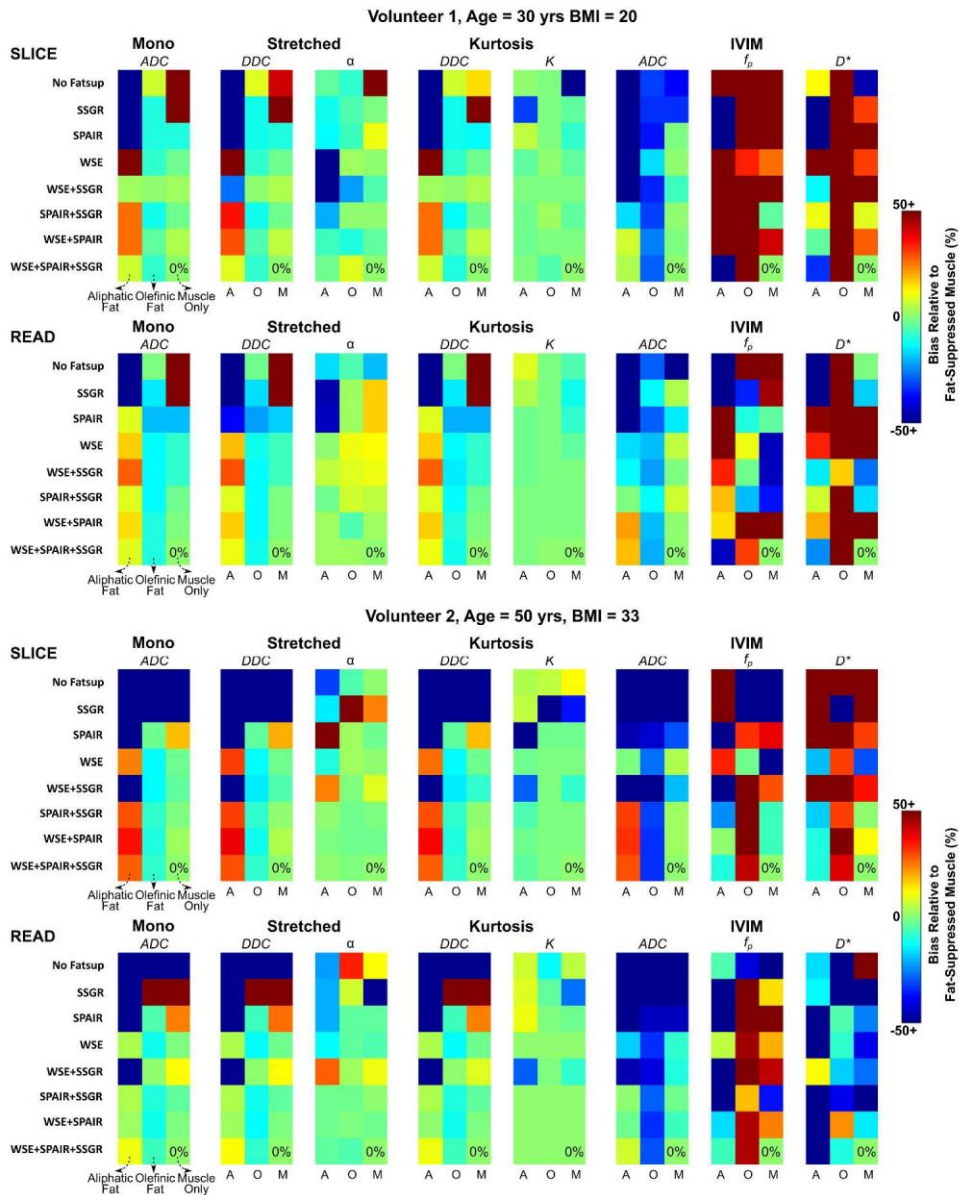


Figure 7. Comparison of in vivo diffusion parameter estimates using different fat suppression combinations. Results were obtained from two healthy volunteers: both male, ages 30 and 51 years, BMI = 20 and 33, and SNR = 83 and 45, respectively. Diffusion sensitization was applied in the slice-select direction, corresponding to the long axes of muscle fibers, and the readout direction, corresponding to their short axes. Plots show data from the green, dark blue, and red ROIs illustrated in Fig. 6: muscle and shifted aliphatic fat (left-hand column, A), muscle and shifted olefinic fat (middle column, O), and muscle alone (right-hand column, M). The color scale shows the relative bias with respect to triple-fat-suppressed muscle; therefore, the bottom-right cell of each plot has an error of 0%. Note that these reference values are different from those of Fig. 5, and ROIs are planned in different muscle regions with possible structural differences. In this case, the muscle signals contain contributions from intramuscular fat, and thus the best measure of pure muscle parameters is obtained when all 3 fat suppression methods are applied together. Parameter biases appear large in muscle, even where there is no visible fat signal; however, the addition of fat suppression methods eliminates this contribution and pushes parameter biases toward zero. The older

1  
2  
3 participant, with higher BMI, shows larger parameter biases in general, but these are sufficiently reduced by  
4 the most effective fat suppression combinations. ADC = apparent diffusion coefficient,  $\alpha$  = stretching  
5 parameter, DDC = distributed diffusion coefficient,  $f_p$  = perfusion fraction, IVIM = intravoxel incoherent  
6 motion, K = kurtosis, SSGR = slice select gradient reversal, SPAIR = spectral attenuated inversion recovery,  
7 WSE = water-specific excitation.

8 Fig. 7

9 412x508mm (300 x 300 DPI)

10  
11  
12  
13  
14  
15  
16  
17  
18  
19  
20  
21  
22  
23  
24  
25  
26  
27  
28  
29  
30  
31  
32  
33  
34  
35  
36  
37  
38  
39  
40  
41  
42  
43  
44  
45  
46  
47  
48  
49  
50  
51  
52  
53  
54  
55  
56  
57

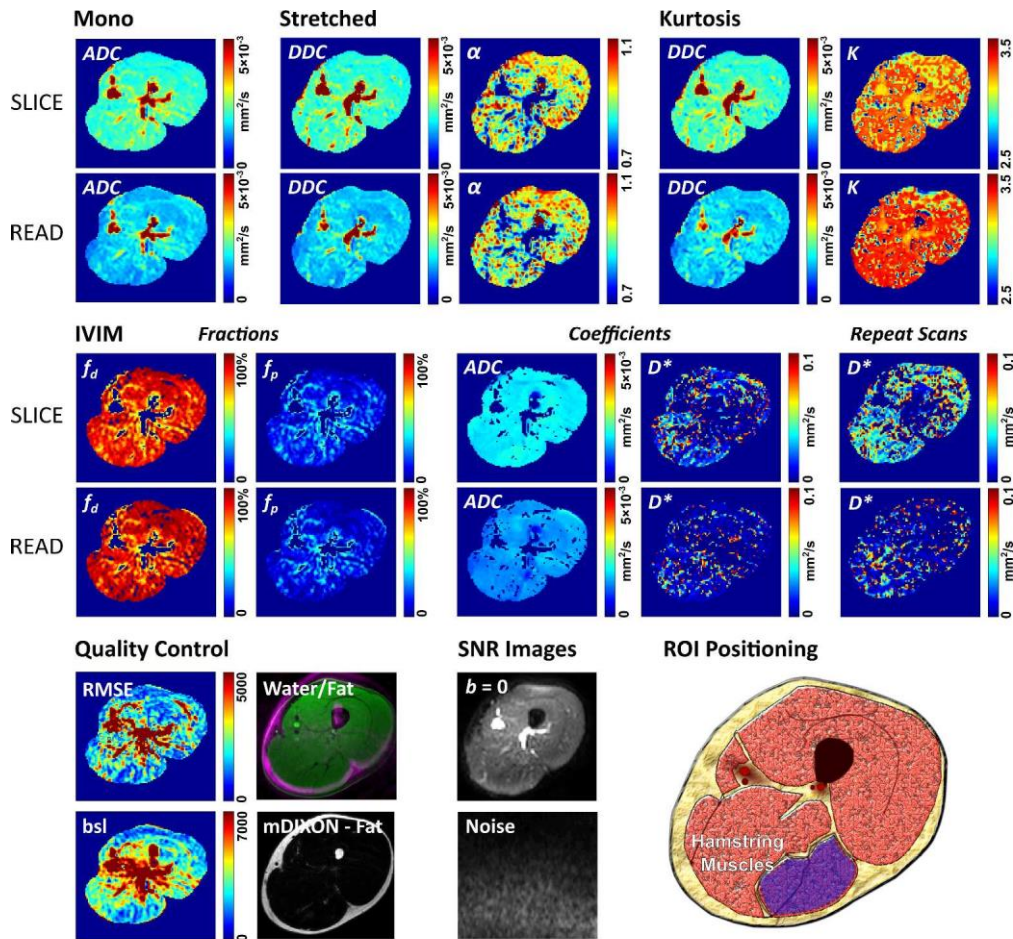


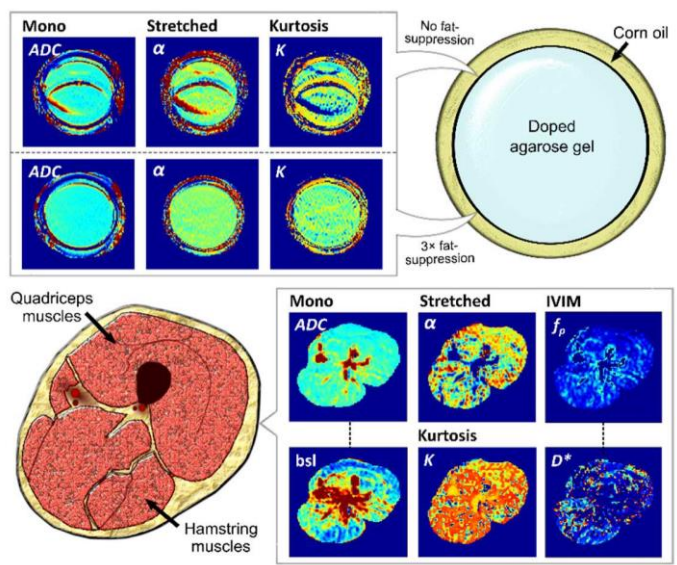
Figure 8: Diffusion parameter maps and region-of-interest (ROI) positioning. Parameter maps were generated from data with a signal-to-noise ratio (SNR) of 45, and are organized by model and diffusion sensitization direction. The following b-values were used: 0, 276, 381, 525, 725, 1000, 1380, 1904, 2627, 3624, and 5000  $\text{s}/\text{mm}^2$  for monoexponential, stretched exponential, and kurtosis models; and 0, 10, 18, 33, 60, 110, 276, 381, 525, 725, and 1000  $\text{s}/\text{mm}^2$  for intravoxel incoherent motion (IVIM). IVIM was fit with constraints on the perfusion fraction,  $f_p$ , and the pseudo-diffusion coefficient,  $D^*$  (0–50% and 5–150  $\times 10^{-3}$   $\text{mm}^2/\text{s}$ , respectively); when parameters converged to these limits, the corresponding pixel was excluded from the map. 'Repeat Scans' highlight variation in  $D^*$  in a second scan session. 'ROI Positioning' shows an example of a region of interest, highlighted in purple, used to calculate the parameter values listed in Table 1. 'Quality Control' figures were used as a guide for ROI definition and to check for intramuscular fat. These include root-mean-square error (RMSE) and baseline offset (bsl) maps, both in signal units, generated from a monoexponential fit with diffusion sensitization in the slice direction; a water/fat image for masking residual fat (a  $b = 5000$   $\text{s}/\text{mm}^2$  image, purple, overlaid on an mDIXON water image, green); and an mDIXON fat image. Also shown are  $b = 0$  and noise images used to calculate SNR. ADC = apparent diffusion coefficient, DDC = distributed diffusion coefficient,  $\alpha$  = stretching parameter, and K = kurtosis.

Fig. 8

369x350mm (300 x 300 DPI)

1  
2  
3  
4  
5 **GRAPHICAL ABSTRACT**  
6

7  
8  
9 Non-Gaussian diffusion models are seeing  
10 increased application in muscle, but their  
11 sensitivity to lipids and noise has not been  
12 systematically investigated. Here, Gaussian  
13 (monoexponential, IVIM) and non-Gaussian  
14 (kurtosis, stretched exponential) models are  
15 evaluated under different noise and fat-  
16 suppression conditions via simulations,  
17 phantom studies, and in vivo experiments. A  
18 combination of three fat suppression  
19 techniques gave the smallest parameter  
20 biases, and use of a baseline offset reduced  
21 model sensitivity to fat; data acquired as  
22 such show non-Gaussian diffusion behavior  
23 in muscle.  
24  
25  
26  
27  
28  
29  
30  
31  
32  
33  
34  
35  
36  
37  
38  
39  
40  
41  
42  
43  
44  
45  
46  
47  
48  
49



**The effect of noise and lipid signals on determination of Gaussian and non-Gaussian diffusion parameters in skeletal muscle**

D. Cameron, M. Bouhrara,  
D.A. Reiter, K.W. Fishbein,  
S. Choi, C.M. Bergeron, L.  
Ferrucci, and R.G. Spencer\*.

# Supplementary Material

## The Effect of Noise and Lipid Signals on Determination of Gaussian and Non-Gaussian Diffusion Parameters in Skeletal Muscle

Donnie Cameron, Ph.D.<sup>1,2</sup>

Mustapha Bouhrara, Ph.D.<sup>1†</sup>

David A. Reiter, Ph.D.<sup>1†</sup>

Kenneth W. Fishbein, Ph.D.<sup>1</sup>

Seongjin Choi, Ph.D.<sup>1</sup>

Christopher M. Bergeron, A.S.<sup>1</sup>

Luigi Ferrucci, M.D., Ph.D.<sup>1\*</sup>

Richard G. Spencer, M.D., Ph.D.<sup>1\*</sup>

<sup>1</sup>*National Institute on Aging, National Institutes of Health, Baltimore, Maryland, USA.*

<sup>2</sup>*Norwich Medical School, University of East Anglia, Norwich, UK.*

†,\* These authors contributed equally to this work.

**Corresponding Author Info:** Richard G. Spencer, M.D., Ph.D., NIH/National Institute on Aging, Intramural Research Program, BRC 04B-116, 251 Bayview Boulevard, Baltimore, MD 21224. E-mail: [spencer@helix.nih.gov](mailto:spencer@helix.nih.gov).

## SUPPLEMENTARY METHODS

### Modeling of Lipid and Noise Signals

Each model described in the main text was investigated with regards to suitable lipid and noise compensation terms. Monoexponential, stretched exponential (SE), kurtosis, and intravoxel incoherent motion (IVIM) fitting functions were each applied with: 1) no offset; 2) with a baseline offset,  $\varepsilon$ ; and 3) a baseline offset plus a noise parameter,  $\xi$ . Furthermore, each of these variants were assessed with a range of maximum  $b$ -values,  $b_{max}$ , in order to assess their performance with or without high  $b$ -value sampling. For the reader's convenience, each of the fitting functions are listed here.

**Base Fitting Functions.** The simplest diffusion-weighted imaging (DWI) fitting functions assessed consisted of the monoexponential, SE, kurtosis, and IVIM functions without a baseline offset or noise correction, as follows.

- *Monoexponential:*

$$S = S_{0,muscle} \exp(-bADC), \quad (S1)$$

where  $S$  is the observed signal,  $S_{0,muscle}$  is the signal at  $b = 0$ , and  $ADC$  is the apparent diffusion coefficient.

- *Stretched exponential (SX):*

$$S = S_{0,muscle} \exp\left(-bDDC^\alpha\right), \quad (S2)$$

where  $DDC$  is the distributed diffusion coefficient and  $\alpha$  is the stretching parameter, with  $0 \leq \alpha \leq 2$ .

- *Kurtosis:*

$$S = S_{0,muscle} \exp\left(-bDDC + b^2DDC^2(K-3)/6\right), \quad (S3)$$

where  $K$  is kurtosis, with  $K \geq 1$ , and  $K = 3$  indicates monoexponential diffusion.

- *Intravoxel incoherent motion (IVIM):*

$$S = S_{0,muscle} \left( f_p \exp(-bD^*) + 1 - f_p \exp(-bADC) \right), \quad (S4)$$

a biexponential fitting function where  $f_p$  is the perfusion fraction and  $D^*$  is the pseudo-diffusion coefficient. This was the IVIM function that was used in the main text.

**Baseline Offset.** A baseline offset,  $\varepsilon$ , was added to each fitting function to compensate for lipid signals and noise. This modifies the observed signal,  $S$ , as follows:

$$S_{bsl} = S + \varepsilon, \quad (S5)$$

creating four new functions. These were the functions applied in the main text, except for IVIM.

**Noise Correction.** A noise parameter,  $\xi$ , was included in addition to the baseline offset to further compensate for noise signals, as described by Jones and Bassler (2004). This can serve to mitigate biases in the baseline offset fitting functions when no lipid signals are present. The baseline offset models are modified as follows:

$$S_{\text{bsl+noise}} = \sqrt{\kappa_{\text{bsl}}^2 + \xi^2}, \quad (\text{S6})$$

creating another 4 functions, for a total of 12 variants.

### Numerical Simulations

Simulations were run using methods similar to those described in the main text. Firstly, diffusion signal decays were generated as per Equations S1–S4 using the following input values:  $ADC = 2.0 \times 10^{-3} \text{ mm}^2/\text{s}$ ,  $DDC = 2.0 \times 10^{-3} \text{ mm}^2/\text{s}$ ,  $K = 3.3$ ,  $f_p = 10\%$ ,  $D^* = 25.0 \times 10^{-3} \text{ mm}^2/\text{s}$ , and  $\alpha = 0.9$ .

Constant baseline offsets were added to these data to produce fat signal fractions of 0–25%, in steps of 0.25%, relative to the fat-free,  $b = 0$  signal amplitude, with the range of fat fractions being chosen to correspond to values seen experimentally with a typical DWI acquisition.

For each fat fraction, zero-mean Gaussian noise, with standard deviation (SD)  $\sigma$ , was added to both the real and the imaginary parts of the complex signal to produce a range of signal-to-noise ratios (SNRs) defined by  $S(0)/\sigma$ . Magnitude data were generated for  $SNR = 1–50$ , in steps of 0.5, each with 250 noise realizations, and noiseless data were generated for the case of infinite SNR.

Data were then fit using each of the functions described in the ‘Modeling of Lipid and Noise Signals’ section, using the same set of  $b$ -values listed in the main text: 0, (IVIM 10, 18, 33, 60, 110), 276, 381, 525, 725, 1000, 1380, 1904, 2627, 3624, and 5000  $\text{s}/\text{mm}^2$ . However, separate analyses were performed to investigate how each fitting function was affected by the choice of  $b_{\text{max}}$ . To this end, additional curve fits were performed using subsets of the aforementioned  $b$ -values, where  $b_{\text{max}}$  was chosen as 1000, 1380, 1904, 2627, 3624 or 5000  $\text{s}/\text{mm}^2$ , where a larger  $b_{\text{max}}$  implies a greater number of points for fitting. For each of these analyses, the bias and dispersion of parameter estimates were calculated according to Equations 8 and 9 in the main text.

It should be noted that IVIM signal decay curves were log-transformed and subjected to a linear fit (up to  $b = 1000 \text{ s}/\text{mm}^2$ ) to estimate  $(1 - f_p)$  and  $ADC$  prior to curve fitting with a bi-exponential function. These parameters were inserted into the bi-exponential fit as fixed terms; thus,  $ADC$  and  $f_p$  were not affected by the inclusion of baseline offset and noise parameters.

Furthermore, in these analyses, IVIM bi-exponential fitting was also investigated for  $b_{\max}$  up to 5000 s/mm<sup>2</sup>, unlike in the main text where the IVIM model used  $b_{\max} = 1000$  s/mm<sup>2</sup>.

### Estimating the Effect of Lipids on Monoexponential Fitting in an Aging Cohort

To explore the potential influence of lipid signals on results reported in the literature, additional simulations were run with the  $b$ -value scheme used by Galbán et al. (2007). These simulations were identical to those described in ‘Numerical Simulations’, except for the following differences: only monoexponential signal decays were generated, with  $ADC = 2.0 \times 10^{-3}$  mm<sup>2</sup>/s; the range of fat signal fractions was 0–50%, in steps of 1%; the SNR range was 1–50, in steps of 1; 250 noise realizations were generated; and simulated data were log-transformed and fitted with a first-degree polynomial, using Galbán’s  $b$ -value scheme ( $b = 0$  and 400 s/mm<sup>2</sup>).

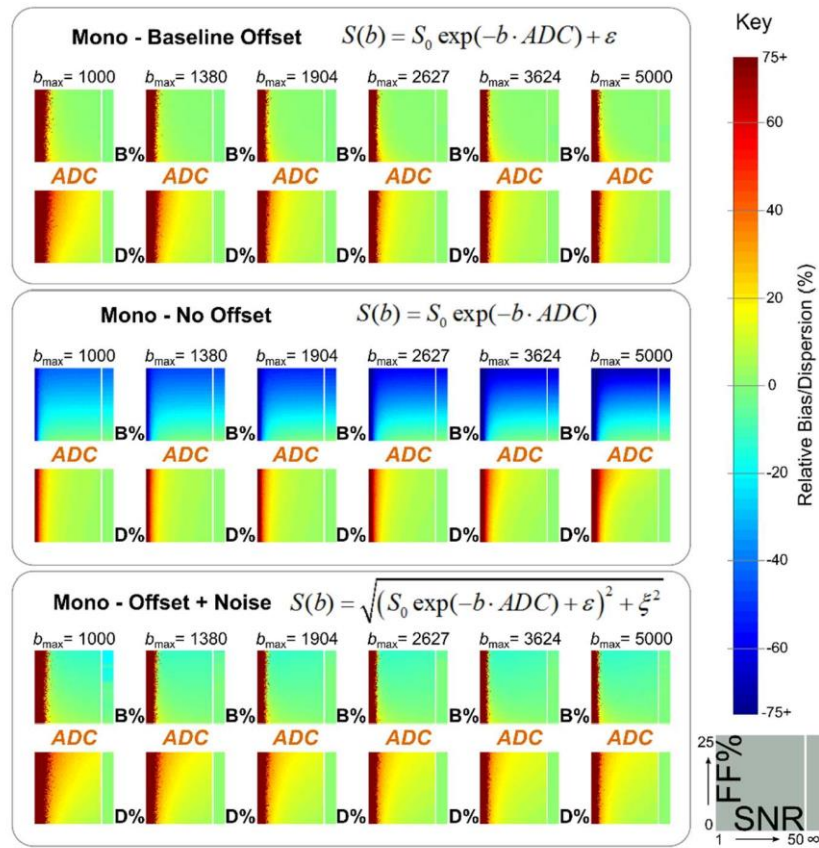
## SUPPLEMENTARY RESULTS & DISCUSSION

Colored matrix plots for each model are shown in Supp. Figs. 1-4, arranged according to their respective base model: monoexponential, SE, kurtosis, and IVIM. Furthermore, plots are subdivided by fitting function, the equations for which are shown alongside the data.

### Numerical Simulations

**Base Fitting Functions.** When baseline offset and noise parameters were excluded from fitting,  $ADC$  and  $DDC$  estimates were strongly, negatively biased by lipid signals for all four models, with the bias becoming more pronounced for higher values of  $b_{\max}$ . However, when lipid content was less than ~3% and SNR was greater than 10, the bias was near-zero. In general, diffusion coefficients showed similar bias trends across all models; dispersion typically approached an asymptote at SNR~5, decreasing with increasing  $b_{\max}$  for the kurtosis model, remaining relatively constant with  $b_{\max}$  for the SX model, and increasing with  $b_{\max}$  for monoexponential  $ADC$ —see Supp Fig. 1.

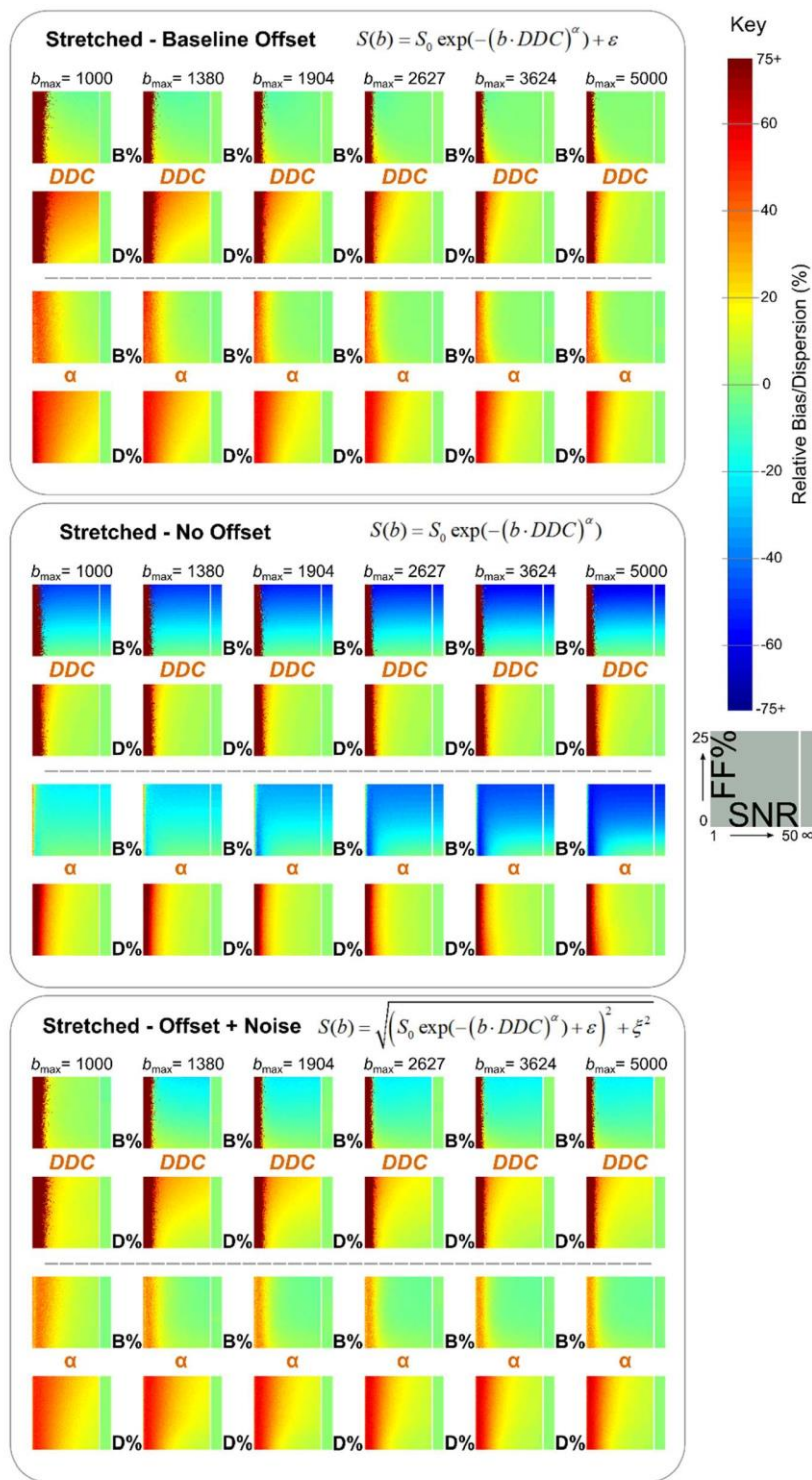
Kurtosis  $DDC$  estimates were the least biased by lipid signals, particularly for low  $b_{\max}$  (Supp. Fig. 3). This may be due to the  $K$  parameter fitting the lipid baseline—an interpretation that is supported by the concomitant increase in  $K$  estimation bias for these data. Generally, the bias in  $K$  was consistent across the range of  $b_{\max}$  values, being dominated by poor detection of the kurtosis model’s quadratic term at low  $b_{\max}$ , and by lipid-related errors for high  $b_{\max}$ . The dispersion in  $K$  estimates decreased gradually with increasing  $b_{\max}$ .



**Supplementary Figure 1: Bias and dispersion in monoexponential parameters with and without a baseline offset in Monte-Carlo simulations.** Colored matrix plots show relative bias ( $B\%$ ) and dispersion ( $D\%$ ) of estimated apparent diffusion coefficients (input  $ADC = 2 \times 10^{-3} \text{ mm}^2/\text{s}$ ). Results are shown for fits incorporating a baseline offset, fits with no offset, and fits with an offset plus noise correction. Individual matrix plots are shown with SNR along the x-axis (1-50 in increments of 1), with a separate column for infinite SNR, and fat signal fraction on the y-axis (0-25% in steps of 1%).

Turning to the SX model's  $\alpha$  parameter (Supp. Fig. 2), this showed trends in estimation bias that were similar to those for the diffusion coefficients, with bias worsening with increasing  $b_{\max}$ . The dispersion in  $\alpha$  was small and consistent across the  $b_{\max}$  range.

For the IVIM model (Supp. Fig. 4), linear fitting of the log of the diffusion signal produced  $ADC$  and  $f_p$  estimates that were strongly sensitive to lipid signals, with the latter showing large bias and dispersion even for fat fractions of 2-3%. The pseudo-diffusion coefficient,  $D^*$ , showed a monotonic relationship with fat fraction, though the slope of this relationship changed sign as a function of SNR. though its dispersion was typically  $>100\%$  for most simulated SNRs. Its dispersion worsened slightly with increasing  $b_{\max}$ , while bias minorly improved.



**Supplementary Figure 2: Bias and dispersion in stretched exponential parameters with and without a baseline offset in Monte-Carlo simulations.** Colored matrix plots show relative bias (B%)

and dispersion (D%) of estimated distributed diffusion coefficients (input  $DDC = 2 \times 10^{-3} \text{ mm}^2/\text{s}$ ), and stretching parameters, (input  $\alpha = 0.9$ ). Results are shown for fits incorporating a baseline offset, fits

with no offset, and fits with an offset plus noise correction. Individual matrix plots are shown with SNR along the x-axis (1-50 in increments of 1), with a separate column for infinite SNR, and fat signal fraction on the y-axis (0-25% in steps of 1%).

**Baseline Offset.** After adding a baseline offset parameter, without a noise term, *ADC* and *DDC* estimates were relatively unbiased for all fat-fractions. However, a bias was observed at low SNRs and low fat fractions, particularly for monoexponential *ADC* (Supp. Fig. 1.) and *SX DDC* (Supp. Fig. 2), where this effect persisted up to SNR~30. Dispersion in diffusion coefficient estimates was generally larger when a baseline offset parameter was included; however, higher  $b_{\max}$  values provided a better baseline fit, with dispersions at  $b_{\max} = 5000 \text{ s/mm}^2$  being similar to those for data fit with no baseline offset or noise parameters.

Much like for diffusion coefficient parameter estimation, addition of an offset mostly eliminated fat-related bias in  $\alpha$  and  $K$  (Supp. Figs. 2 and 3); however, the minimum SNR needed to avoid large dispersion increased when an offset was added, particularly for low values of  $b_{\max}$ . Furthermore, for  $K$ , the addition of an offset flipped the bias polarity—leading to strong, negative biases at low SNRs, particularly for low  $b_{\max}$  values.

Adding a baseline offset to the IVIM fitting function caused the polarity of the  $D^*$  estimation bias to flip at low SNRs (Supp. Fig. 4), becoming strongly positive; however, at high SNRs it was performed similarly to the base IVIM fitting function. The dispersion in  $D^*$  was similar in magnitude to that in data fit without a baseline offset. Fat fractions of 10% or greater led to a large negative bias and small dispersion in  $D^*$  estimation, producing large errors in  $D^*$ .

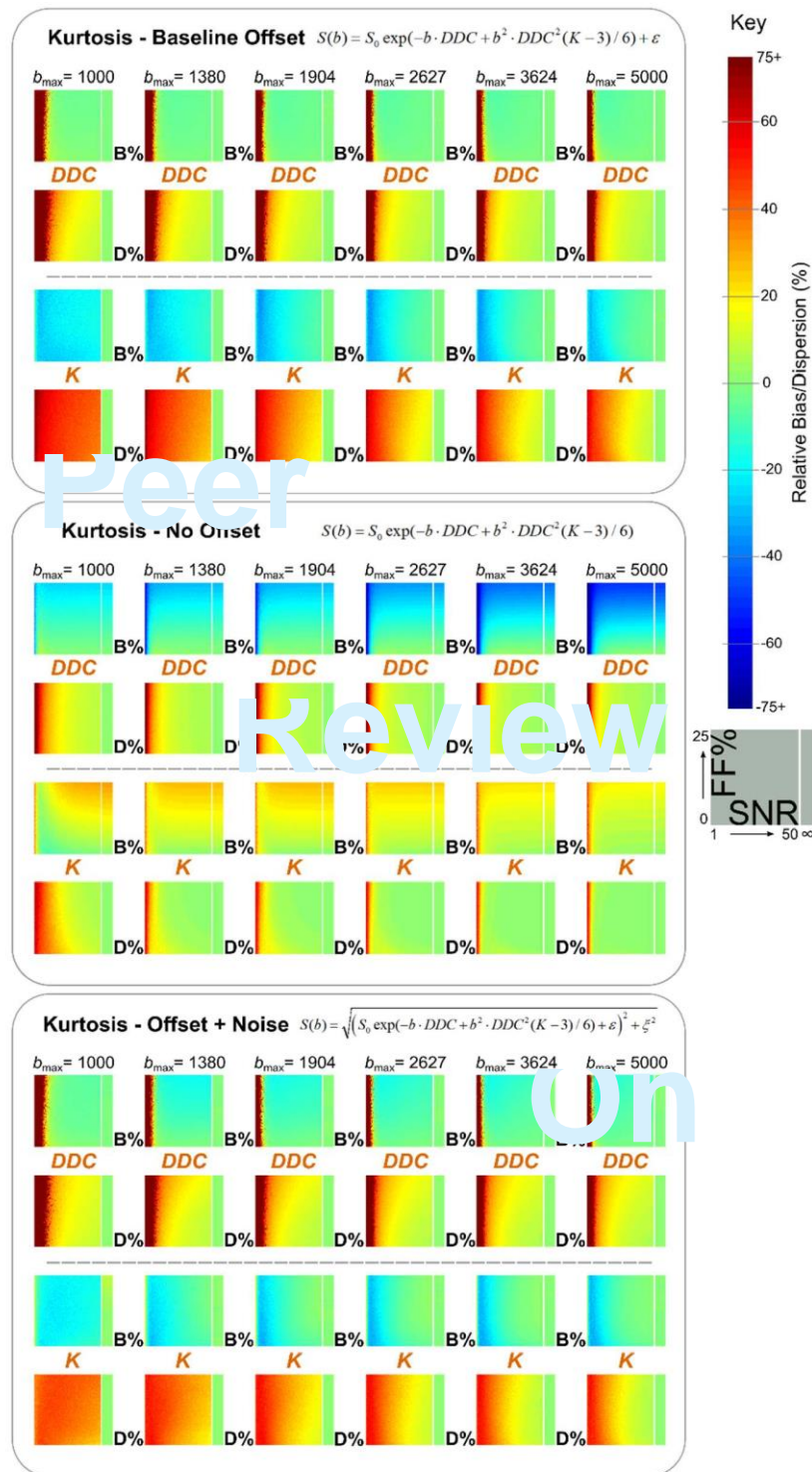
**Noise Correction.** Upon fitting with both a baseline offset and a noise parameter, *ADC* and *DDC* estimates became slightly more sensitive to fat-related bias versus fitting with an offset alone, though the noise related bias at 0% fat was reduced. For monoexponential *ADC* (Supp. Fig. 1) and *SX* and kurtosis *DDC* (Supp. Figs. 2 & 3) dispersion was slightly larger than for data with a baseline offset alone, though the use of higher  $b_{\max}$  values was seen to mitigate this effect.

The use of baseline offset and noise parameters also slightly increased the sensitivity of  $\alpha$  to fat-related bias at higher fat fractions, but the bias at low fat fractions was improved (Supp. Fig. 2). Dispersion was similar to that observed for the ‘offset only’ model.

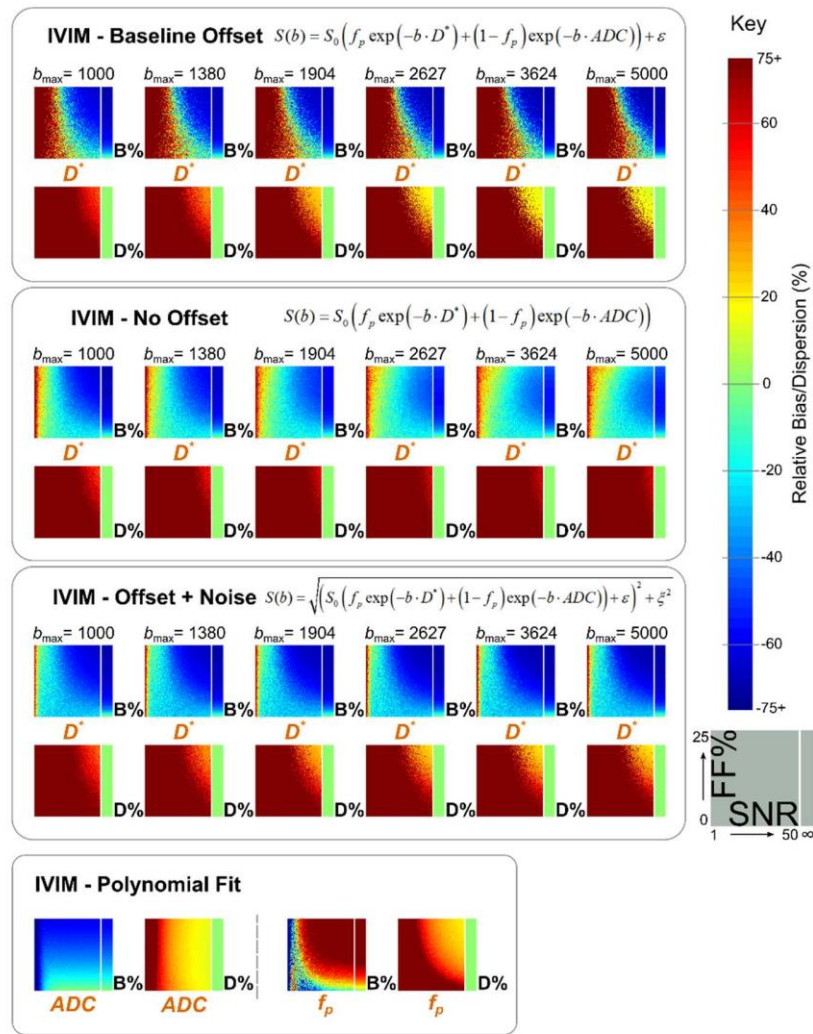
Addition of a noise parameter made very little difference to the bias and dispersion in  $K$  (Supp. Fig. 3), relative to data fit with an offset only.

Dispersion in  $D^*$  estimation (Supp. Fig. 4) was little influenced by the addition of a noise parameter; however, the bias in  $D^*$  was more similar to that seen for the base IVIM fitting function data rather than the ‘baseline offset’ data.

**Summary.** In general, diffusion parameter estimation performs well without baseline offset or noise parameters provided the fat fraction is sufficiently low, and SNR is sufficiently high. The choice of  $b_{\max}$  values only becomes important when estimating kurtosis, or when considerable fat



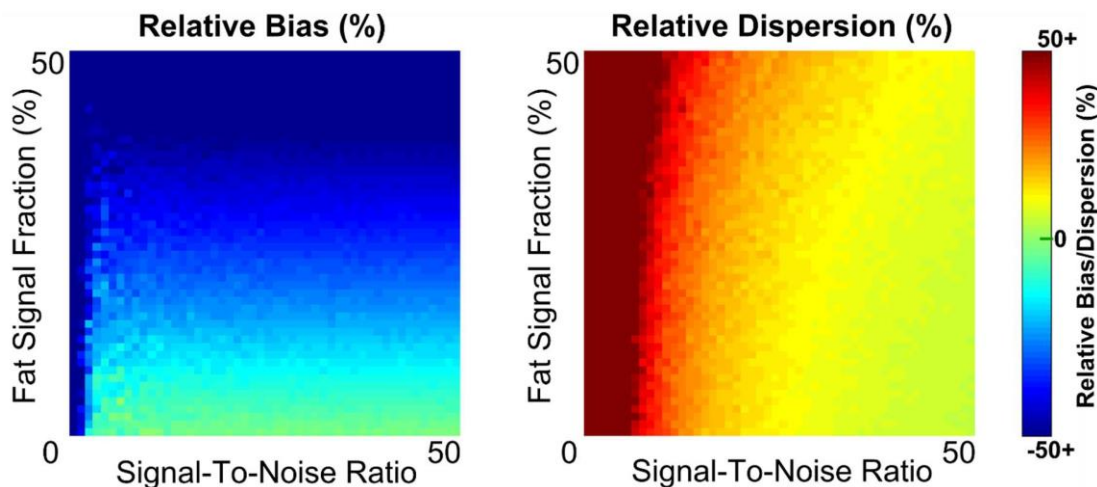
**Supplementary Figure 3: Bias and dispersion in kurtosis parameters with and without a baseline offset in Monte-Carlo simulations.** Colored matrix plots show relative bias (B%) and dispersion (D%) of estimated distributed diffusion coefficients (input DDC =  $2 \times 10^{-3} \text{ mm}^2/\text{s}$ ), and kurtosis, (input  $K = 3.3$ ). Results are shown for fits incorporating a baseline offset, fits with no offset, and fits with an offset plus noise correction. Individual matrix plots are shown with SNR along the x-axis (1-50 in increments of 1), with a separate column for infinite SNR, and fat signal fraction on the y-axis (0-25% in steps of 1%).



**Supplementary Figure 4: Bias and dispersion in intravoxel incoherent motion (IVIM) parameters with and without a baseline offset in Monte-Carlo simulations.** Colored matrix plots show the relative bias (B%) and dispersion (D%) of estimated apparent diffusion coefficients (input  $ADC = 2 \times 10^{-3} \text{ mm}^2/\text{s}$ ), perfusion fractions (input  $f_p = 10\%$ ), and pseudo-diffusion coefficients (input  $D^* = 25 \times 10^{-3} \text{ mm}^2/\text{s}$ ). Results are shown for fits incorporating a baseline offset, fits with no offset, and fits with an offset plus noise correction. Individual matrix plots are shown with SNR along the x-axis (1-50 in increments of 1), with a separate column for infinite SNR, and fat signal fraction on the y-axis (0-25% in steps of 1%).

contamination is present: the greater the  $b_{\max}$ , the more sensitive parameter estimation is to lipid signals. Noise bias in experimental data could be mitigated by removing high  $b$ -values, as shown by Marschar et al. (2015); however, particular care must be taken with the kurtosis model, where high  $b$ -values are needed to detect kurtosis.

Use of a baseline offset parameter becomes useful for high SNR DWI data that are known to contain lipid signals, small or large: for example, in DWI signal decays that are generated from



**Supplementary Figure 5: Monte-Carlo simulation data showing bias and dispersion in the apparent diffusion coefficient (ADC) for a low  $b$ -value acquisition.** Colored matrix plots show the relative bias and dispersion of estimated ADC, with parameters as follows: monoexponential decay, input  $ADC = 2.0 \times 10^{-3} \text{ mm}^2/\text{s}$ , linear fit to log-transformed data with  $b = 0$  and  $400 \text{ s}/\text{mm}^2$ , and 250 noise realizations. Plots show SNR increasing along the x-axis and fat signal fraction (%) increasing along the y-axis, both from one to fifty in increments of one. The color map for relative bias and dispersion was limited to  $\pm 50\%$  to improve color contrast between different fat signal fractions. As shown, small changes in fat fraction can lead to relatively large negative biases in ADC estimates.

regions of interest rather than on a pixel-by-pixel basis. However, use of a baseline offset term typically led to a noise-related bias at low SNRs and  $\sim 0\%$  fat fraction, and was detrimental to  $D^*$  estimation—leading to large biases of varying sign without any improvement in dispersion.

Further addition of a noise parameter to DWI fitting functions mitigates the noise bias seen at  $\sim 0\%$  fat fraction with baseline offset fitting functions; however, this leads to small increase in lipid sensitivity, with no improvement to bias or dispersion in  $D^*$  estimation for the IVIM model.

In general, DWI fitting functions incorporating baseline offset and noise parameters may be of use for data with middling SNR and low to middling fat fractions.

### Estimating the Effect of Lipids on Monoexponential Fitting in an Aging Cohort

Fitting the logarithm of a monoexponential signal decay using a first-degree polynomial led to substantial lipid sensitivity in estimated ADCs (Supp. Fig. 5). Bias in ADC estimation was consistent across the range of SNRs investigated, though it approached an asymptote at  $SNR \sim 5$ ; bias worsened with increasing fat fraction at the rate of  $-10\%$  for every  $5\%$  fat fraction added.

Dispersion was more dependent on SNR, only slightly increasing as fat fraction increased.